Journal: Catalysis Today,

Manuscript ID: CATTOD-D-22-00348

Manuscript Type: Article

Title: "Hydrophobic RWGS catalysts: valorization of CO_2-rich streams in presence of CO/H_2O"

Author(s): P. Tarifa, M. González-Castaño, F. Cazaña, A. Monzón and H. Arellano-García.

Dear Editor,

The authors appreciate the suggestion of the reviewers of the revised manuscript with ID code: CATTOD-D-22-00348. Afterward, all the comments have been completed to improve the scientific discussion of the results.

As previous revision, all the comments, and the answers, text modifications and clarifications are listed below. Additionally, changes have been highlighted in yellow in the revised version of the manuscript file.

Editor can find the respond to the reviewers' comments in the following paragraphs. In addition, the modifications made in the manuscript have been also included here.

Reviewers' comments:

Reviewer #2: The manuscript CATTOD-D-22-00348R1 has been improved as the Authors have been taken into account several comments from the Reviewers. However, several points of concern still remain; in my opinion, some of them could be solved. In its present form, I cannot recommend for publication in Catalysis Today journal.

Some relevant points are:

1.-The passivation treatment should be clearly referred to the CO_2 treatment.

-Answer: The authors acknowledge the review's comment. However, the passivation includes N_2 treatment overnight as well as subsequence CO_2 treatment. To clarify this point, the corresponding part has been rewritten.

"Upon cooling down, the catalyst was passivated under N_2 overnight followed by a mixture of 16% of CO_2 (balanced with N_2 with a total flow of 250 mL/min) for 1 h."

2.-The TPR profiles should be shown and commented accordingly.

-Answer: As the authors comment in previous revision, the TPR indicates very low H_2 consumptions. The major H_2 consumed is cause of the decomposition occurred at higher temperatures than the synthesis one, i.e. 700 ºC. Even though, the TPR profile have been included in the revised manuscript as well as its comment in the text as follows:

The TPR profiles of the samples are shown in Fig. 6. It is shown two peaks at around 400 and 700 ºC. According to XRD results, the peak located at 400 ºC is attributed to the reduction of Fe oxidized during the passivation since the major part of Fe remains reduced after the synthesis. Thus, the H_2 consumed in this part corresponds to less than 0.4 µmol reinforcing the latter. In addition, due to the catalysts are prepared at 700 ºC, a greater peak shown at higher temperatures is attributed to the further decomposition of the catalysts.

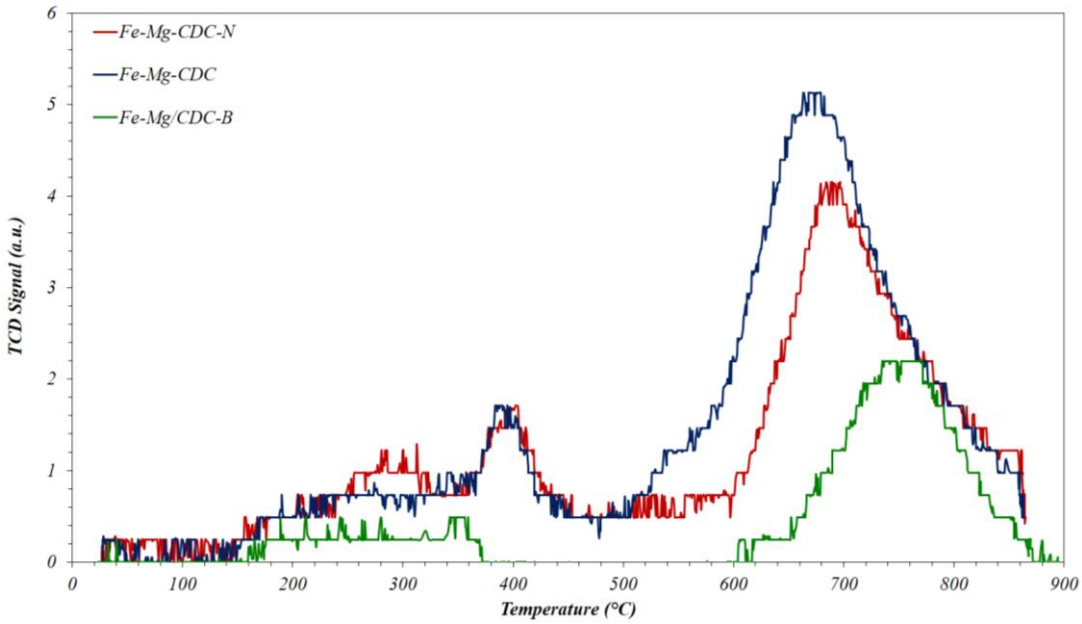

Fig. 6. TPR profiles of as-prepared catalysts.

The procedure were also included in the experimental section.

3.-The pristine CDC material must be separately reported for textural and compositional data.

-Answer: We appreciate the suggestion. The required analysis can be found in the supplementary information file and referenced in the revised version of the manuscript.

Table SI.1. Elemental analysis and textural properties of pristine supports.

Support	C[a] (*wt.*%)	H[a] (*wt.*%)	N[a] (*wt.*%)	B[b] (*wt.*%)	O[c] (*wt.*%)	S_{BET} (m^2/g)	Pore volume (cm^3/g)	Micropore volume (%)	d_{pore} (nm)
N-CDC	88.24	2.12	4.52	-	5.12	7	0.019	17	1.1
CDC	95.07	1.43	0.59	-	2.91	482	0.219	87	1.1
B-CDC	74.93	1.65	0.40	6.89	16.13	2	0.002	49	13.4

[a]weight percentage obtained from elemental analysis
[b]weight percentage obtained from TGA-Air data
[c] weight percentage obtained from mass balance

4.-The behavior of CDC, and derived N- and B- materials as for CO_2-TPD must be reported.

-Answer: The authors acknowledge this suggestion. Certainly, it is necessary to a better understanding of the catalysts. The corresponding figure has been included in the supplementary information as Fig. SI. 2 and the reference has been included in the manuscript as follows:

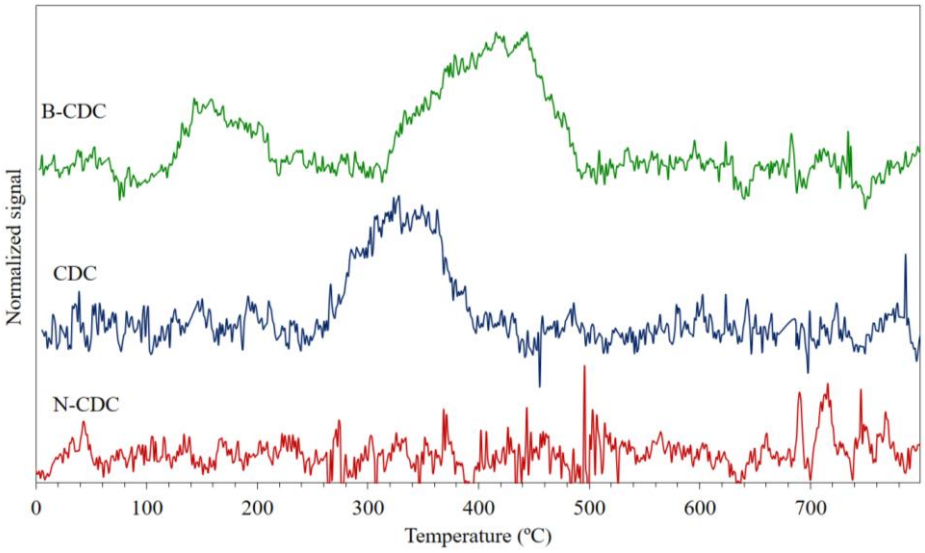

Fig SI.2. Normalized CO_2 profile resulted from CO_2-TPD analysis of the reduced supports. The amount of CO_2 desorbed was 10 µmol/g in case of B-CDC and 4 µmol/g in case of CDC.

"On the other hand, all samples exhibited a CO broad peak (no shown in supports, Fig.SI.2) from 600 ºC composed by two contributions attributed to phenol and carbonyl groups."

5.-The XPS peak for Mg^{2+} must be clearly discussed.

-Answer: In order to clarify this point, the Mg 2s and Mg KLL signals have been included in the supplementary information along with more explanation in the revised manuscript in section 3.3 (XPS), in 3.4(catalytic activity) and in conclusions as follows:

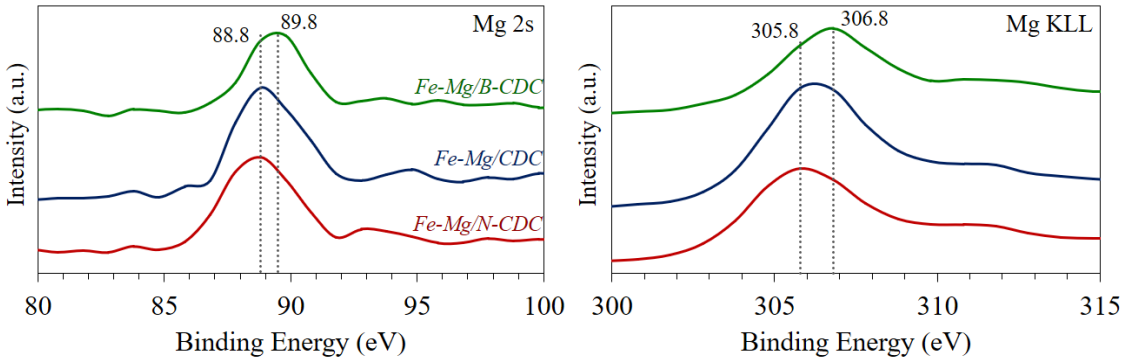

Fig SI.3. XPS spectra of Mg 2s and satellite signal of as-prepared catalyst.

"While the addition of N has low impact on Fe and Mg binding energies, B leads to a shift to higher binding energies in comparison with Fe-Mg/CDC indicating stronger interaction between those atoms. Indeed, given the higher electronegativity of boron with respect to Fe and Mg, it is produced an electron transfer from Fe and Mg to B leading to an electron deficiency in central atoms [39] which hinders CO_2 adsorption. The latter is in accordance with signals of Mg 2s and Mg KLL shown in supplementary information (Fig. SI.3)."

"Under H_2/CO_2 feed streams, Fe-Mg/CDC exhibited higher CO productivity being these *ca*. three times higher the values reached by the Fe-Mg/B-CDC catalyst. For the RWGS reaction, the adsorption and activation of CO_2 constitutes a limiting step [2] which is indorse by basicity of the catalysts. Analogously, the poorer RWGS performance might be related to minor CO_2 adsorption cause by, on the one hand, a partial block of the basic active sites by surface B_2O_3 domains and, on the other hand, the higher binding energies showed by Fe and Mg (Fig.5)."

"The activity of the catalysts was measured under RWGS conditions (500 °C, H_2/CO_2 = 4/1) and the impact of CO and H_2O species as co-reactants in the feed was evaluated. Fe-Mg/CDC reaches higher CO productivity under model conditions (CO_2/H_2) most likely due to its higher basicity. In the presence of CO, the electronic properties of the Fe-Mg/CDC catalyst seem to also promote CO adsorption thereby depleting its RWGS

performance. On the contrary, CO adsorption is greatly inhibited by B_2O_3 enabling less accused drops on the CO_2 conversion values. On the other hand, the presence of water provokes a major impact in Fe-Mg/B-CDC since electron deficiency on Fe and Mg could lead to stronger adsorption of H^+/OH^- species on the catalyst."

6.-The EDS-STEM and TEM results must commented in this work and, at least, reported as supplementary material.

-Answer: Truly, EDS-STEM results reinforces TEM images and clearly show the nanoparticles. Then, these results are now included in the supplementary information in Fig. SI.2. Also, it has been properly referenced in the manuscript as follows:

"On the other hand, despite the differences in the macrostructure, TEM images (shown on the right side of Fig.3) and EDS-STEM results (shown in Fig. SI.1) show that the metallic nanoparticles are well dispersed on the carbonaceous support in all cases."

Highlights

- N- or B- doping improves the Fe-Mg/CDC performance for the RWGS in presence of CO and H_2O.
- Fe-Mg/CDC attained higher CO productivity due to promoted CO_2 adsorptions.
- A higher ratio of Mg/Fe could improve the resistance against water.
- B-doped catalyst displays higher conversion in presence of CO.

Graphical Abstract

Click here to access/download;Graphical Abstract (for review);4-Graphical Abstract_Catalysis Today_Tarifa.pdf

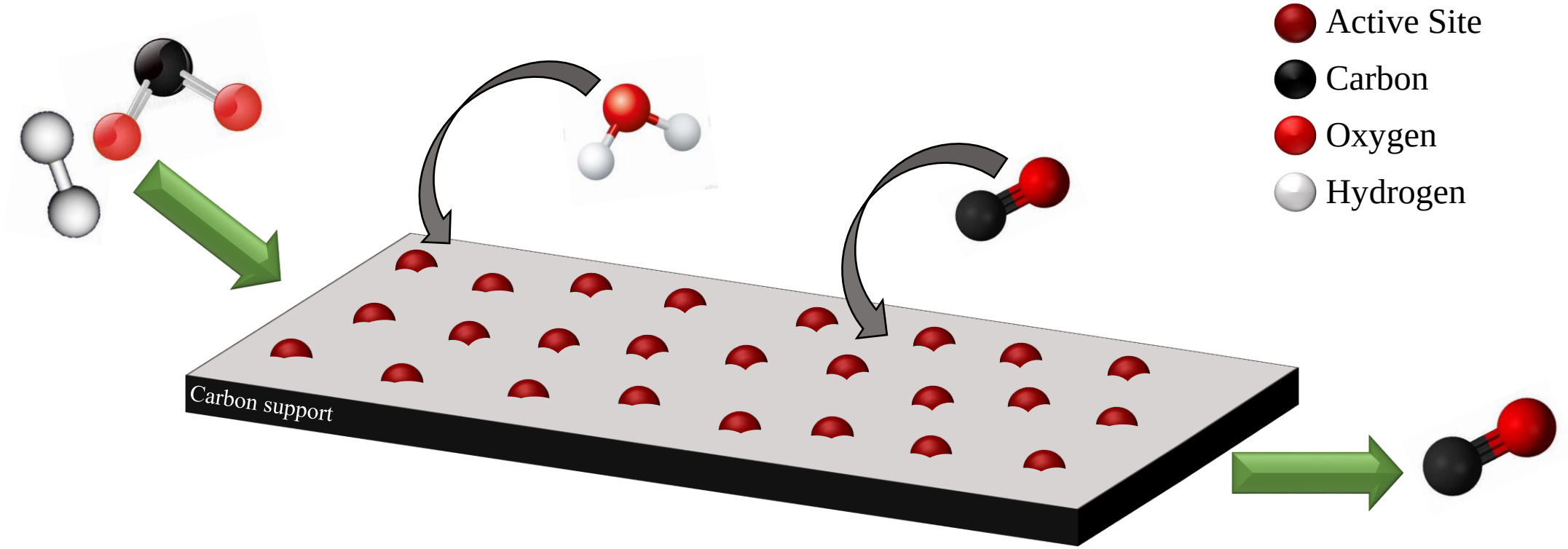

Manuscript for review Click here to view linked References

Hydrophobic RWGS catalysts: valorization of CO_2-rich streams in presence of CO/H_2O

P. Tarifa[a,b], M. González-Castaño[a], F. Cazaña[b], A. Monzón[b], H. Arellano-García[a].

[a] Department of Process and Plant Technology. Brandenburg University of Technology (BTU) Cottbus-Senftenberg, Platz der Deutschen 1, 03046 Cottbus, Germany

[b] Department of Chemical and Environmental Engineering, Institute of Nanoscience and Materials of Aragón (INMA), CSIC-University of Zaragoza, E-50018 Zaragoza, Spain

corresponding author: ptarifa@unizar.es, gonzalez@b-tu.de

Keywords: Reverse Water Gas Shift, biogas, H_2O, Fe catalysts, hydrophobic, doped-carbon supports.

Abstract

Nowadays, the majority of the Reverse Water Gas Shift (RWGS) studies assume somehow *model* feedstock (diluted CO_2/H_2) for syngas production. Nonetheless, biogas streams contain certain amounts of CO/H_2O which will decrease the obtained CO_2 conversion values by promoting the forward WGS reaction. Since the rate limiting step for the WGS reaction concerns the water splitting, this work proposes the use of hydrophobic RWGS catalysts as an effective strategy for the valorization of CO_2-rich feedstock in presence of H_2O and CO. Over Fe-Mg catalysts, the different hydrophilicities attained over pristine, N- and B-doped carbonaceous supports accounted for the impact on the activity of the catalyst in presence of CO/H_2O. Overall, the higher CO productivity (4.12 μmol/(min·m^2)) attained by Fe-Mg/CDC in presence of 20% of H_2O relates to hindered water adsorption and unveil the use of hydrophobic surfaces as a suitable approach for avoiding costly pre-conditioning units for the valorization of CO_2-rich streams based on RWGS processes in presence of CO/H_2O.

1. Introduction

Syngas is a key compound for the industrial production of multiple chemicals such as ammonia, alcohol, ethanol, acetic acid, or formaldehyde in addition to synthetic fuel [1–7]. The depletion of conventional sources such as natural gas, liquid hydrocarbons, fossil oil or coal [2,8,9] along with the associated carbon footprint characteristics of the traditional production routes motivate the need for the development of alternative and more sustainable sources of syngas. Biogas constitutes one such an unconventional and renewable source that has the potential to enable a delocalized conversion of CO_2-rich residues into syngas mixtures. Coupling thermocatalytic CO_2 valorization units to biogas streams derived from biomass treatment plants represents one of the central strategies projected towards the implementation of more sustainable energy systems [2–6]. In this frame, the combination of Reverse Water Gas Shift (RWGS) with Fischer-Tropsch reaction units has been proposed the most economically feasible process towards the generation of syngas [10–12].

RWGS is an endothermic equilibrium reaction in which CO_2 and H_2 are converted into CO along with H_2O molecules ($CO_2+H_2=CO+H_2O$) at temperatures higher than 700 ºC. Currently, the vast majority of RWGS studies devoted to the development of long-life efficient catalysts considers *model* feedstock composed by diluted CO_2/H_2 [13,14]. Nevertheless, although only in lower concentrations, biogas streams contain several side components like CH_4, CO, and H_2O in concentrations depending on the biomass source as well as the treatment [15–22]. For instance, disregarding Sulphur compounds and particulate matter, the average biogas composition derived from gasification units (recognized as the most easily scalable technology for biomass treatment) might be envisaged in a range of 8-57%CO_2, 5-40%CO, 3-50%H_2, 0-20%CH_4, 7-17%H_2O and N_2 [10,23–27]. Thus, insights into the influence of minor compounds commonly present in biogas should enable the design of catalytic systems capable of operating under more realistic feedstock and reducing the number of pre-conditioning units required for the biogas valorization. Recently, González-Arias [28] evaluated the performance of Cu-MnO_x

based catalysts under *model* and simulated biomass-derived streams (22% CO_2,66% H_2, 1% CO, 1% CH_4 and N_2 balanced). Different optimal MnO_x contents were found depending on the reaction atmosphere. Thus, compared to *model* feedstock (22% CO_2, 66% H_2), higher amounts of MnO_x maintained higher conversion values in presence of CH_4/CO fractions most likely due to improved resistances against coking phenomena.

Therefore, the incorporation of adequate amounts of redox promoters enhanced the performance of the RWGS catalysts under simulated biomass-derived feedstocks [28,29]. However, the CO_2 conversion drops observed in presence of CO were also associated to favored forward WGS reaction, in concordance to Le Chatelier principle. A potential strategy for constricting the negative impact that CO and H_2O induces over the CO_2 conversion values might rely on inhibiting the adsorption of the reactants on the catalyst surface and, in consequence, the forward WGS reaction. Given that the rate limiting step of the WGS reaction involves the water dissociation step, the use of a hydrophobic system should inhibit the extent at which the WGS reaction occurs, permitting higher CO_2 conversion rates [30,31].

In this sense, the use of carbonaceous supports like CNT, activated carbon, carbon spheres or Cellulose Derived Carbon (CDC) arises as an appealing approach. Being widely proposed as catalytic supports [3,32–35], carbon materials remain cost-effective and can be easily prepared from biomass conferring a renewable character [36]. Remarkably, the easily tunable textural properties [37] and functionalities of CDC supports provide tools for specific design of the catalyst depending on the final application [38]. Thus, the incorporation of heteroatoms combined to adequate surface treatments tailor the type and concentration of functional oxygenated groups affecting the acid-base or hydrophobic character thereby governing the overall catalyst behavior [32,39–41].

This study investigates the use of hydrophobic RWGS supported catalysts as an approach for the valorization of biogas streams containing H_2O and CO as undesired constituents. Among the different metals usually proposed for the RWGS reaction (Cu and Fe) [42], Fe was preferred

because of its cost-effectiveness, optimal activity and selectivity and higher thermal stability. [2,43–47]. Moreover, Mg was added as electronic promoter so the CO_2 adsorption and coke resistance were indorsed [48]. The hydrophobicity of the systems was tuned by doping the CDC supports with N and B species [49–51]. Hence, (10 wt.%)Fe-(10 wt.%)Mg catalysts supported over pristine, N-doped and B-doped CDC supports were prepared and tested for the RWGS reaction in absence and presence of H_2O and CO impurities. The chosen H_2O and CO percentages were extrapolated considering biogas feedstock derived from gasification processes. The lower conversion drops exhibited by the N-doped CDC catalyst emphasize that tailoring the hydrophobic character of the catalysts constitutes an optimal strategy towards the development of RWGS catalysts with higher tolerances towards CO/H_2O fractions.

2. Experimental

2.1. Synthesis of the catalysts

The samples were prepared by wetness impregnation of cellulose (fibers cellulose from *Sigma Aldrich*) with an aqueous dissolution with $Fe(NO_3)_3 \cdot 9H_2O$ from *Sigma Aldrich* and $Mg(NO_3)_2 \cdot 6H_2O$ from *Panreac* as metal precursors. The metal loading was fixed at 3.5%wt. of Fe with respect to the dried cellulose, along with an atomic ratio of Fe:Mg=3:7. After the impregnation, the solid was placed in a horizontal furnace and dried at 100 °C for 12 h in 50 mL/min of N_2. Afterwards, thermal decomposition was carried out under reducing atmosphere (50% H_2 balanced with N_2) at 700 °C for 3 h using a heating rate of 50 °C/min. Upon cooling down, the catalyst was passivated under N_2 overnight followed by a mixture of 16% of CO_2 (balanced with N_2 with a total flow of 250 mL/min) for 1 h. This catalyst was labelled as Fe-Mg/CDC. In addition, hydrophobic and hydrophilic catalysts were prepared adding urea or boric acid to the aqueous dissolution (6 g of urea crystal from *Panreac* and 1.6g of boric acid from *STREM Chemicals*, respectively). Then, the solid was treated following the steps

previously described. In this case, the catalysts were labelled as Fe-Mg/N-CDC and Fe-Mg/B-CDC, respectively.

2.2.Characterization techniques

The metal content of the samples was measured by inductively coupled plasma mass spectrometry (ICP-MS) with Thermo Scientific equipment. The metal content was also evaluated by TGA-Air analysis. The determination of C, H and N content on the catalysts was carried out using a Leco CHN628 elemental analyzer. The thermal stability was analyzed in Air using a METTLER Toledo STA/SDTA 851e thermogravimetric instrument. The TGA-Air experiments were conducted using around 1 mg of sample placed in a 40 μL crucible. Then, the sample was heated up to 900 ºC with a heating rate of 10 ºC/min. Since carbonaceous support is burned off under oxidative atmosphere, the metallic percentage of the samples was calculated from the weight of the remaining ashes assuming elements at their higher oxidation state (Fe_2O_3, MgO and B_2O_3 in each case). Given that the nominal molar ratio of the metal precursors used during the catalyst preparation is known, the composition of the catalysts was estimated.

XRD diffractograms were obtained by a Siemens D-5000 (45 kV, 40 mA) diffractometer equipped with Cu anode (kα radiation, λ=0,1542 nm). The diffractograms were acquired in the 5º to 90º 2θ range with 0.02º counting step and a step time of 4 s. The phase composition was determined by using an ICDD database and the High Score Plus (PANalytical) software. The crystallite size (CS) of each species was calculated using the Scherrer's equation [52].

The textural properties of the samples were analyzed by N_2 adsorption-desorption isotherms carried out at 77 K using a Tristar 3000 equipment from *Micromeritics Instrument Corp*. The surface area was calculated through Brunauer−Emmett−Teller (BET) method. On the other hand, the total pore volume along with the average pore diameter were obtained by the Horváth−Kawazoe method, while the *t*-plot method was employed to determine the

microporous volume. Finally, Barrett-Joyner-Halenda (BJH) method was used to obtain the pore size distribution.

Scanning electron microscopy (SEM) micrograph images were captured in a FEI Inspect F50 microscope operating at 10 kV microscope. Moreover, transmission electron microscopy (TEM) micrograph images were acquired in a FEI Tecnai T-20 microscope operating at 200kV.

CO_2-TPD analyses (Temperature Programmed Desorption) were performed in a ChemBet PULSAR from *Quantachrome instruments*. 50 mg of sample were placed in a U-shape reactor. Over the pre-reduced samples cooled down in inert atmosphere, CO_2 was adsorbed at room temperature exposing the sample to a flow of 15% CO_2 diluted with He for 40 min. The CO_2 specie physisorbed were removed in He flow. Afterwards, CO_2-TPD was carried out heating up to 700 °C with a heating rate of 15 °C/min. The TCD as well as mass spectrometer signals with mass-to-charge ratio (m/z) of 2, 4, 15, 28 and 44 were acquired continuously.

The chemical composition of the surface was analyzed by X-ray photoelectron spectroscopy (XPS) in a Kratos Axis ULTRA spectrometer using non-monochromatic Al Kα radiation (hν = 1486.7 eV). The spectra were analyzed using CASA XPS software by applying a Shirley-type background.

The reducibility of the samples was analyzed by Temperature Programme Reduction (TPR) in a ChemBet equipment from Anton Paar. 50 mg of sample was charged in U-shape quartz reactor. The samples were heated from room temperature up to 900 ºC at 10 ºC/min using 10% of H_2 balanced with He. TCD and mass spectrometer signals with mass-to-charge ratio (m/z) of 2, 4, 15, 28 and 44 were recorded continuously.

2.3.Catalytic activity

The catalysts diluted with SiC were placed in a fixed-bed tubular reactor (8 mm of inner diameter). The amount of catalysts was calculated in order to maintain the CO_2/ Fe ratio constant (CO_2 molar flow/Fe mass was fixed to 3.02 mol $CO_2 \cdot g_{Fe}^{-1} \cdot h^{-1}$) being GHSV 12000 h^{-1} in all cases. Prior to the reaction, the catalyst was reduced at 700 °C for 1 h using 40% of

H_2 balanced with N_2 (100 mL/min of total flow). Afterwards, the reaction was carried out at 500 °C feeding 15% of CO_2 and 60% of H_2 in all cases. In addition to that, between 3-15% of CO or 5-20% of H_2O were also co-fed. The composition of the exhausted gases was analyzed by a gas chromatographer model HP 6890 equipped with a ShinCarbon ST column. The CO productivity was calculated through the Eq.1. Additionally, the impact of CO and H_2O in the activity was calculated as the variation of the productivity respect to the CO productivity obtained under H_2/CO_2 streams following the Eq.2.

$$CO\ productivity\left(\frac{\mu mol}{\min \cdot m^2}\right) = \frac{F_{CO,\text{out}}}{m_{cat} \cdot S_{BET}} \quad \text{(Eq 1)}$$

$$\Delta CO\ productivity(\%) = \frac{CO\ prod._{\text{CO/H}_2O} - CO\ prod._{H_2/CO_2}}{CO\ prod._{H_2/CO_2}} \quad \text{(Eq 2)}$$

3. Results and discussion

3.1 Chemical and structural composition of the fresh catalysts

Table 1 shows the chemical composition obtained for the samples. According to TGA, the decomposition of the impregnated cellulose results in metal percentages higher than the nominal ones (3.5%wt. Fe and 3.6%wt. Mg) resulting in ca. 10%wt. of Fe along with 10%wt. of Mg in all cases. The Fe percentage obtained by ICP results are very close to that confirming the metallic content in the final catalysts. In addition to that, in Table 1 elemental analysis results are also included. As we can see, C and H are quite similar in all samples seeing little differences. On the contrary, Fe-Mg/B-CDC contains 5.89% of B while the N content is higher in Fe-Mg/N-CDC due to the addition of these precursors in the synthesis. In comparison with bare supports, CDC is composed mainly by carbon (see Table SI.1) while N-CDC and B-CDC show higher percentage of O due to the presence of N and B species.

Table 1. Chemical composition and elemental analysis of the fresh catalysts.

Catalyst	Fe[a] (*wt*.%)	Fe[b] (*wt*.%)	Mg[a] (*wt*.%)	B[a] (*wt*.%)	C[c] (*wt*.%)	H[c] (*wt*.%)	N[c] (*wt*.%)	O[d] (*wt*.%)
Fe-Mg/N-CDC	10.4	9.2	10.5	-	53.40	1.49	2.48	21.73
Fe-Mg/CDC	13.3	12.3	13.5	-	48.27	1.39	0.55	22.99
Fe-Mg/B-CDC	9.6	7.5	9.7	5.89	54.36	1.10	0.71	18.64

[a]weight percentages obtained from TGA-Air data
[b]weight percentages obtained from ICP measurements
[c]weight percentage obtained from elemental analysis
[d] weight percentage obtained from mass balance

In addition, the structural composition was analyzed by XRD. The diffractograms displayed in Fig. 1 show common peaks located at 44.7°, 65.0° and 82.3° attributed to metallic Fe along with peaks at 36.1°, 43.0° and 62.0° which correspond to MgO. Also, a broad peak located around 26.1° corresponds to amorphous carbonaceous support, which also appears in all catalysts. Moreover, peaks located at 43.5º, 50.6º and 74.2º are shown in Fe-Mg/B-CDC diffractogram which are attributed to $Fe_{0.94}C_{0.06}$. Regarding heteroatom addition, no nitrogen species are shown in Fe-Mg/N-CDC whereas two peaks appear in the case of Fe-Mg/B-CDC. These peaks, located at 33.5° and 19.9°, correspond to B_2O_3. This fact is due to the N species which are not introduced into the carbon lattice being removed as NO_x volatile compounds. Nevertheless, in case of boric acid, the excess of B-species remains in the catalyst as B_2O_3. In Table 2, the metallic crystal sizes calculated through Scherrer's equation are presented. Thus, metallic Fe as well as MgO manifest similar average crystal size around 38 nm and 8 nm, respectively, in as-prepared catalysts. This indicates that N or B have no significant effect on the dispersion of the metallic nanoparticles.

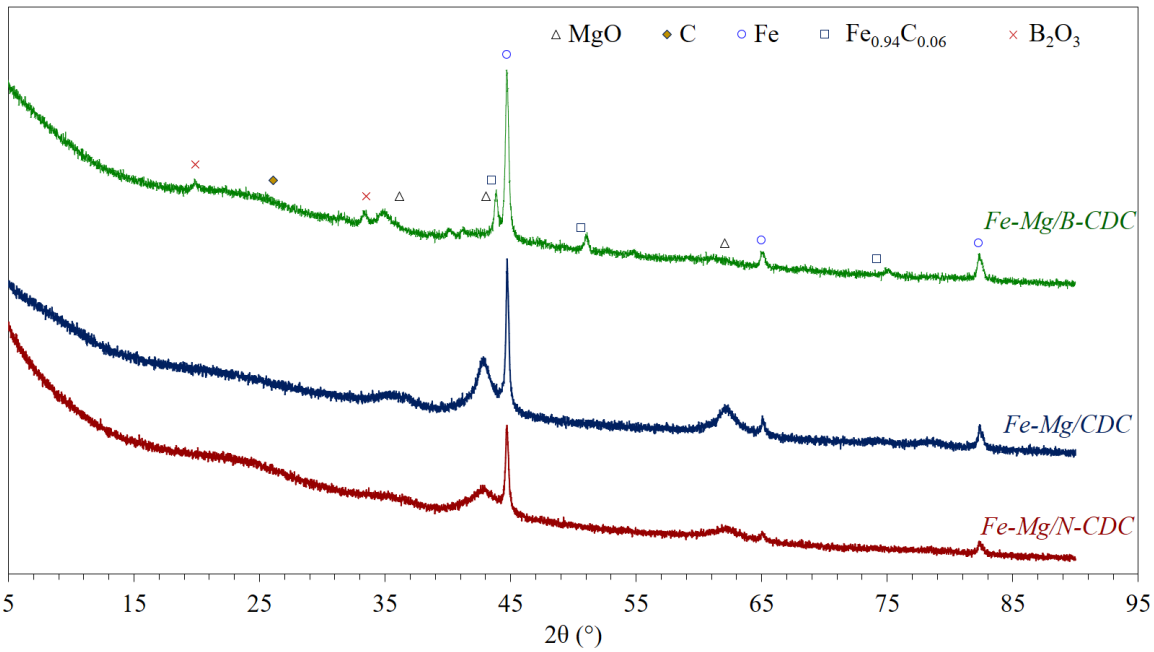

Fig. 1. XRD of the fresh catalysts.

3.2 Textural properties and micrographs of the fresh catalysts

Textural properties were analyzed by N_2 adsorption isotherms and the values obtained are presented in Table 2. Accordingly, the catalysts showed a high surface area and pore volume obtaining minimum values of 320 m^2/g and 0.291 cm^3/g, respectively, with Fe-Mg/B-CDC. In comparison with bare supports, the surface area of Fe-Mg/CDC decreases (see Table SI.1) while, in presence of N or B, surface area of the corresponding catalyst significantly increases due to metals favor the cellulose decomposition. Furthermore, the pore volume distribution displayed in Fig. 2 showed that the catalysts are mainly mesoporous materials. Thus, in comparison with Fe-Mg/CDC, Fe-Mg/N-CDC developed higher surface area as well as microporosity showing smaller average pore diameter, 1.1 nm. On the other hand, although Fe-Mg/B-CDC showed similar microporosity and average pore diameter to Fe-Mg/CDC, its surface area and pore volume decreases likely due to B-species (B_2O_3) provokes a partial block of porosity.

Table 2. Crystal size and textural properties of the fresh catalysts

	Crystal size	Textural properties

Catalyst	Fe[a] (nm)	MgO[a] (nm)	S_{BET} (m^2/g)	Pore volume (cm^3/g)	Micropore volume (%)	d_{pore} (nm)
Fe-Mg/N-CDC	38	8	436	0.330	33	1.1
Fe-Mg/CDC	41	10	388	0.374	25	2.7
Fe-Mg/B-CDC	32	7[b]	320	0.291	28	2.4

[a]calculated through Scherrer equation applied to the peak located at 44.7° for Fe and 43.0° for MgO
[b]calculated through Scherrer equation applied to the peak located at 36.1°

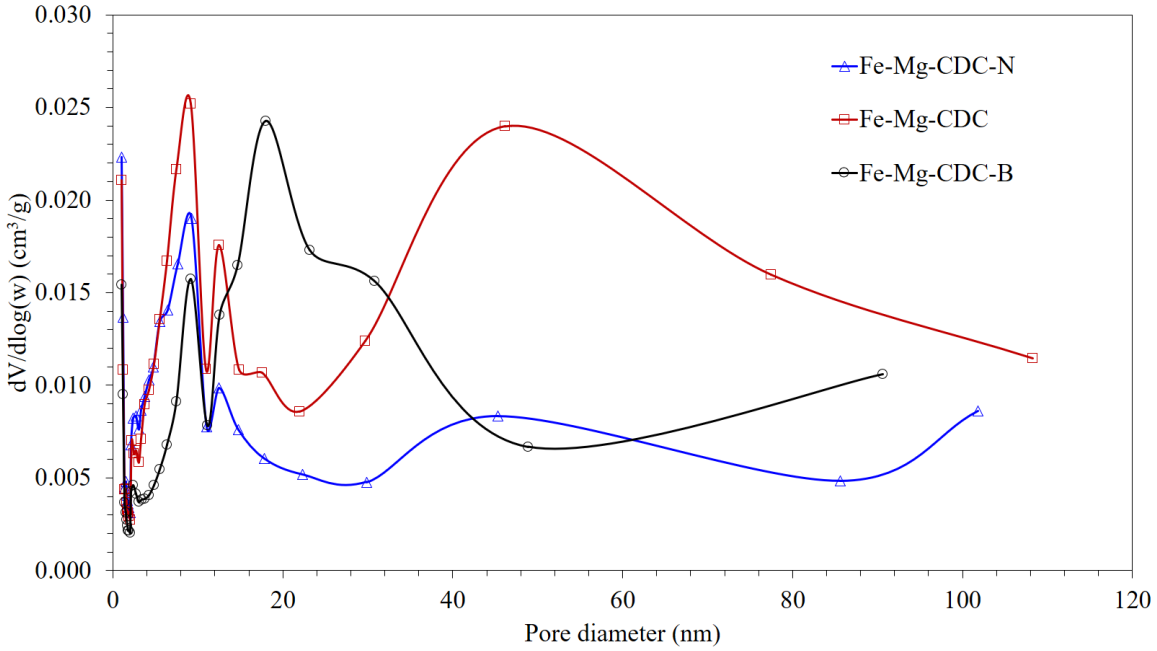

Fig. 2. Pore volume distribution of the fresh catalysts.

SEM images of the fresh catalysts are presented on the left side of Fig.3. There, Fe-Mg/N-CDC (Fig. 3A) revealed a series of intricate cavities on its surface whereas the surfaces of Fe-Mg/CDC and Fe-Mg/B-CDC are softer. Nevertheless, a higher scale image of Fe-Mg/B-CDC (Fig. 3C inset, scale of 1µm) revealed small spheres dispersed on the surface likely corresponding to B_2O_3. On the other hand, despite the differences in the macrostructure, TEM images (shown on the right side of Fig.3) and EDS-STEM results (shown in Fig. SI.1) show that the metallic nanoparticles are well dispersed on the carbonaceous support in all cases. These results are in concordance with the N_2 adsorption results as well as XRD diffractograms discussed previously.

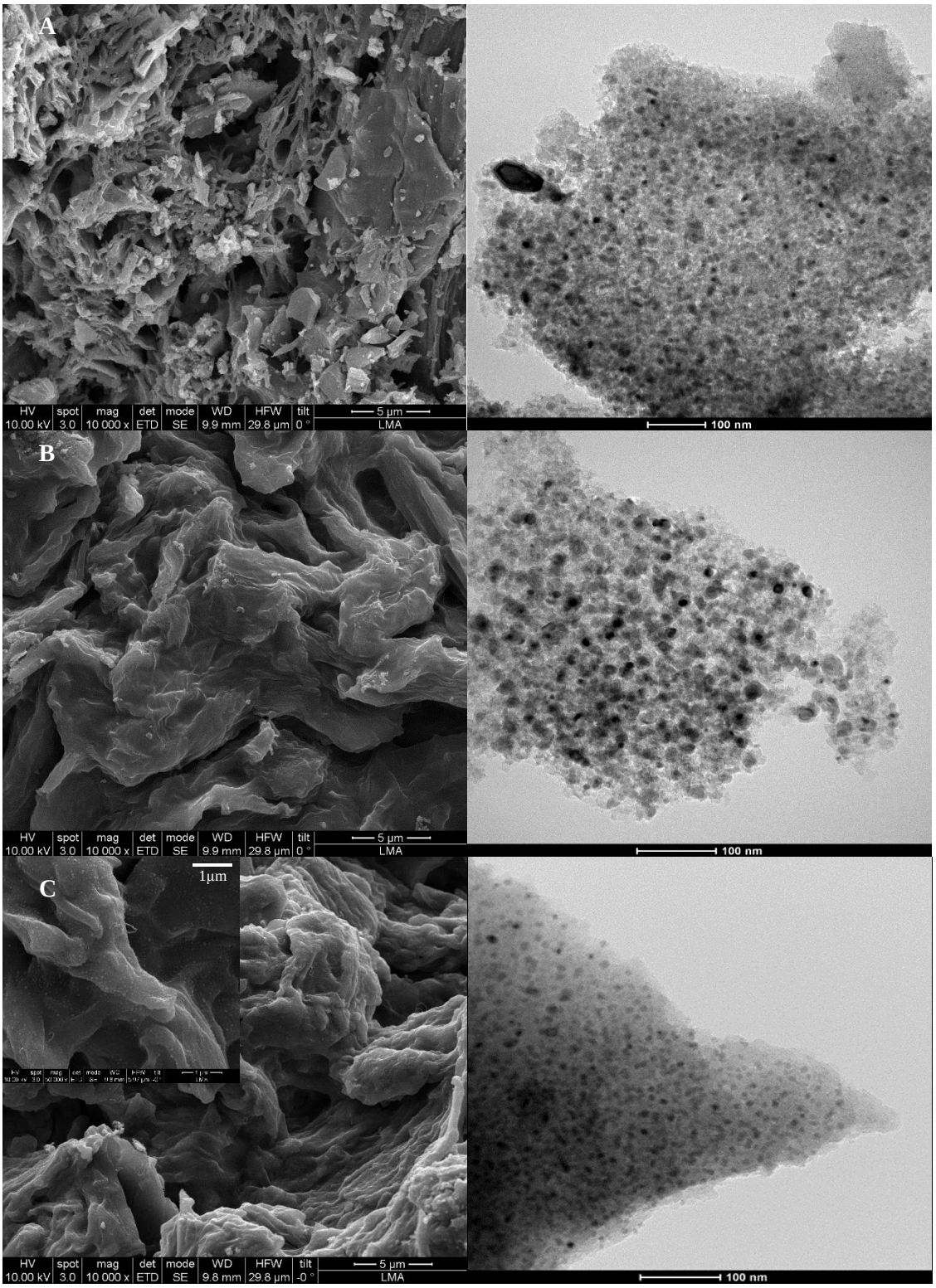

Fig. 3. SEM (left) and TEM (right) images of fresh catalysts: (A) Fe-Mg/N-CDC, (B) Fe-Mg/CDC and (C) Fe-Mg/B-CDC.

3.3 Chemical and redox properties

The CO_2-TPD were used to measure the basicity of the pre-reduced catalysts. In carbon materials, CO_2 and CO are released from the decomposition of the surface oxygen functional groups (OFGs). CO_2 is released at lower temperatures and it is related with acid sites while CO is atributted to basic sites and it appears at higher temperatures [40,53]. Specifically, CO_2 results from carboxylic acids, carboxylic anhydrides and lactones being lactone group more thermally stable. Likewise, CO results from carboxylic anhydrides, phenols, carbonyls and quinone groups [54]. In this work, carboxylic anhydrides were discarded due to CO_2 and CO signals are not overlapped. For Fe-Mg/CDC and Fe-Mg/N-CDC, the observed CO_2 desorption profiles (zoomed in Fig. 4 inset) exhibited a single broad peak located at *ca.* 300 °C which can be ascribed to carboxylic groups and underline the presence of relatively weak adsorption sites. However, the main CO_2 desorption peak observed for the Fe-Mg/B-CDC sample points to moderate-strenght sites and could be associated to the decomposition of lactone species. On the other hand, all samples exhibited a CO broad peak (no shown in supports, Fig.SI.2) from 600ºC composed by two contributions attributed to phenol and carbonyl groups. In case of Fe-Mg/B-CDC, a broader CO peak indicates the presence of stronger sites. Table 3 summarizes the quantification of the CO_2 and CO released along with the basic site density of each catalyst calculated from the CO evolved. Fe-Mg/CDC presents higher basic site density than Fe-Mg/N-CDC likely due to a low content of N remained in the carbon lattice as a result of the high temperature used in the synthesis as is corroborated by XPS results, Fig. 5.

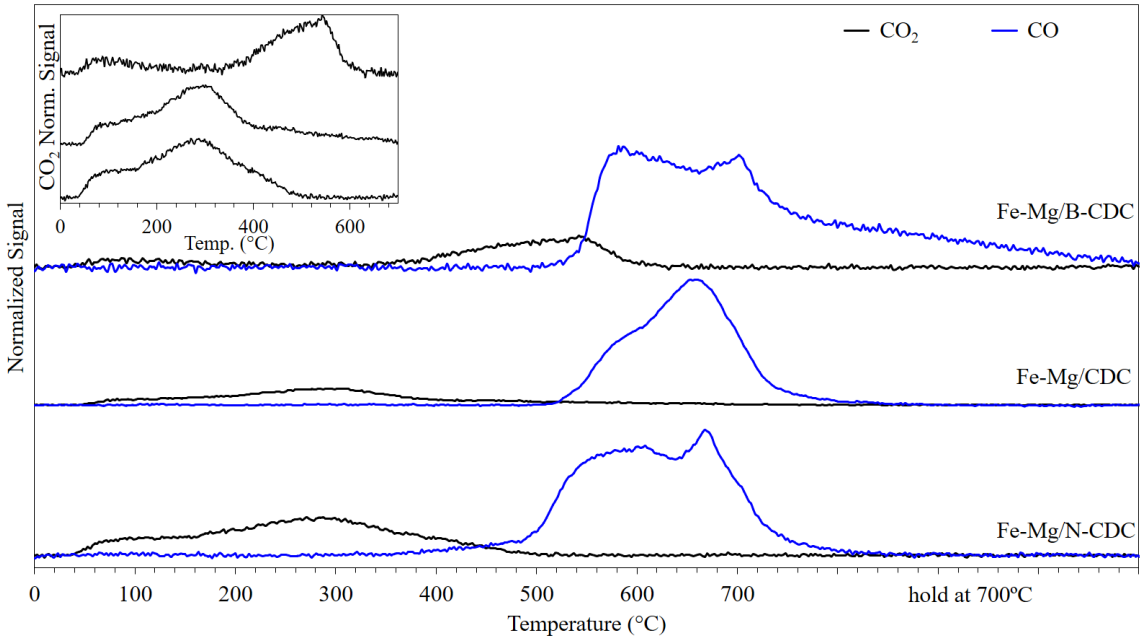

Fig. 4. Normalized CO_2 and CO evolution resulted from CO_2-TPD analysis of the reduced catalysts.

Table 3. Quantification of CO_2-TPD carried out over the pre-reduced catalysts.

Catalyst	Total CO_2 (µmol/g)	Total CO (µmol/g)	Basic site density (µmol/m^2)
Fe-Mg/N-CDC	98	284	0.651
Fe-Mg/CDC	101	556	1.433
Fe-Mg/B-CDC	30	155	0.484

The surface chemical state of the catalysts was identified by XPS analysis. Fig.5 shows XPS spectra of the different atoms involved in each catalyst. In addition, Table 4 shows the atomic percentage obtained from XPS spectra (*i.e.* surface percentages) and TGA-Air test (approximately *at%* bulk). As we can see in Fig. 5, the spectra of Fe 2p exhibits a pair of peaks located around 710.9 eV (Fe 2p3/2) and 724.5 eV (Fe 2p1/2) attributed to Fe^{3+} in Fe_2O_3 [55]. Likewise, the peak located around 1304.0 eV of Mg 1s spectra corresponds to Mg^{2+} [56] as well as the peak located around 193.8 eV of B 1s is attributed to B_2O_3 [39]. This is corroborated by O 1s spectra where the peaks located at 531.9 and 530.3 eV can be identified as O^{2-} from metal oxides and adsorbed O-H [57,58]. Thus, those spectra indicate that Fe, Mg as well as B are

presented as metal oxides while different C-N configurations were found. While the addition of N has low impact on Fe and Mg binding energies, B leads to a shift to higher binding energies in comparison with Fe-Mg/CDC indicating stronger interaction between those atoms. Indeed, given the higher electronegativity of boron with respect to Fe and Mg, it is produced an electron transfer from Fe and Mg to B leading to an electron deficiency in central atoms [39] which hinders CO_2 adsorption. The latter is in accordance with signals of Mg 2s and Mg KLL shown in supplementary information (Fig. SI.3). The atomic percentages, shown in Table 4, indicates that the concentration of Fe is quite low taking into account the atomic percentage in the bulk. Nevertheless, Fe content is higher in Fe-Mg/CDC catalyst. On the other hand, Mg atomic percentages are higher than Fe in all cases being higher also in Fe-Mg/CDC. These results are in concordance with CS found by XRD where Mg is much smaller than Fe and, therefore, more dispersed. Regarding the heteroatoms, only a minor part of N remains into the carbon lattice while B_2O_3 content represents 5.32% of the surface in case of Fe-Mg/B-CDC. This value is rather similar to B content in the bulk (5 %at.) indicating that B is mainly on the surface.

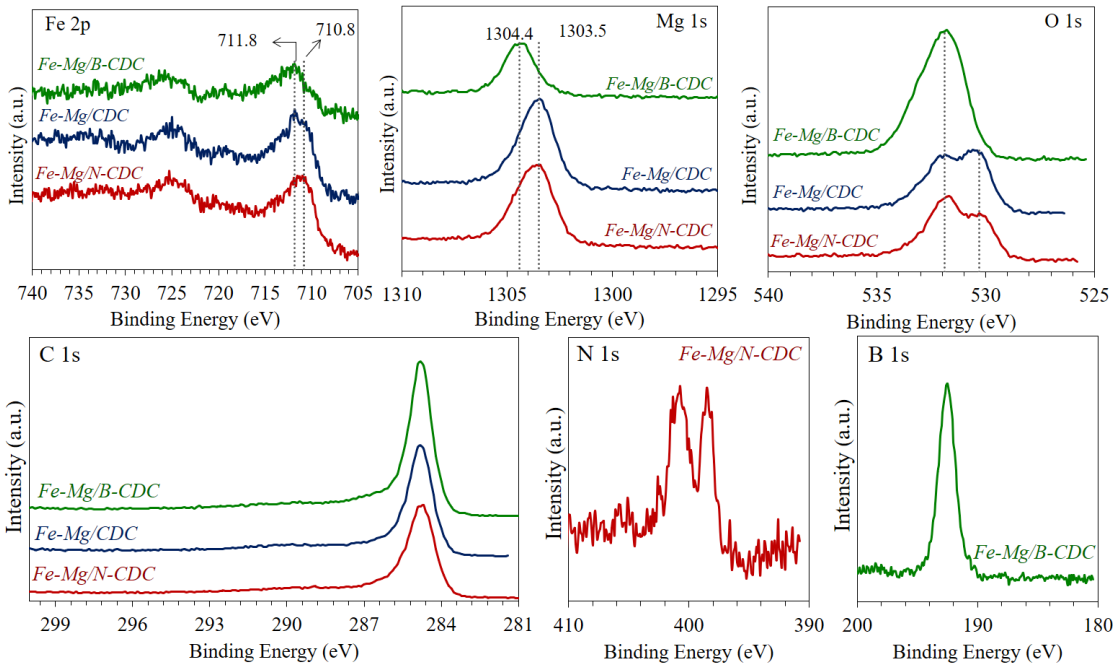

Fig. 5. XPS spectra of as-prepared catalyst.

Table 4. Surface atomic percentages of as-prepared catalyst.

Catalysts	Fe 2p (*at.%*)	Fe_{bulk} (*at.%*)	Mg 2s (*at.%*)	Mg_{bulk} (*at.%*)	C 1s (*at.%*)	O1s (*at.%*)	N or B (*at.%*)	Mg/ Fe	Fe/C ($\cdot 10^3$)
Fe-Mg/N-CDC	0.38	2.57	5.92	6.06	78.8	14.9	1.07	15.6	4.8
Fe-Mg/CDC	0.55	3.44	6.34	8.15	77.51	15.60	-	11.5	7.1
Fe-Mg/B-CDC	0.34	2.35	3.45	5.54	72.06	18.83	5.32	10	4.7

The TPR profiles of the samples are shown in Fig. 6. It is shown two peaks at around 400 and 700 ºC. According to XRD results, the peak located at 400 ºC is attributed to the reduction of Fe oxidized during the passivation since the major part of Fe remains reduced after the synthesis. Thus, the H_2 consumed in this part corresponds to less than 0.4 µmol reinforcing the latter. In addition, due to the catalysts are prepared at 700 ºC, a greater peak shown at higher temperatures is attributed to the further decomposition of the catalysts.

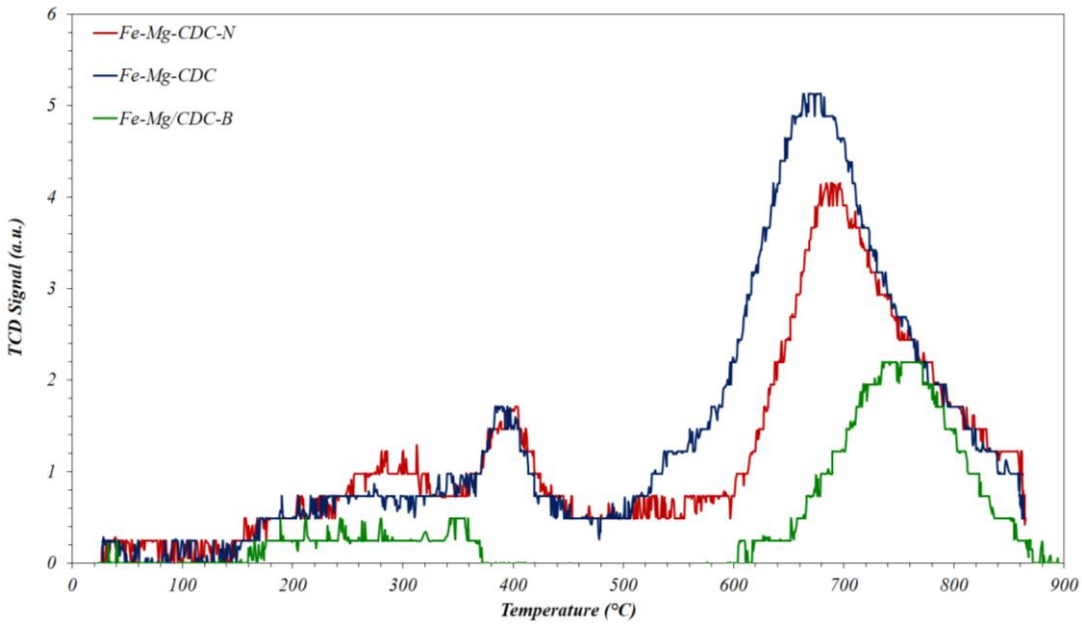

Fig. 6. TPR profiles of as-prepared catalysts.

3.4 Catalytic activity

The productivity to CO per unit of surface exhibited by the catalysts' series at 500 °C under different RWGS reaction atmospheres is shown in Fig. 7 represented by bars. In addition to that, the impact of CO/H_2O on the productivity was calculated as the variation of the

productivity respect to H_2/CO_2 feed stream productivity (dash lines). Under H_2/CO_2 feed streams, Fe-Mg/CDC exhibited higher CO productivity being these *ca*. three times higher the values reached by the Fe-Mg/B-CDC catalyst. For the RWGS reaction, the adsorption and activation of CO_2 constitutes a limiting step [2] which is indorse by basicity of the catalysts. Analogously, the poorer RWGS performance might be related to minor CO_2 adsorption cause by, on the one hand, a partial block of the basic active sites by surface B_2O_3 domains and, on the other hand, the higher binding energies showed by Fe and Mg (Fig.5). Moreover, as it was expected, the addition of CO or H_2O resulted in a drop in the CO yield since the RWGS is an equilibrium reaction and the incorporation of reaction products shift the equilibrium towards the reactants. The incorporation of CO affected in a significant manner the systems with higher RWGS activity suggesting that Fe-Mg/CDC and Fe-Mg/N-CDC samples adsorb efficiently both CO and CO_2 species. Indeed, it is well known that N-containing groups enhance the adsorption of the CO [32,59] whilst B-species greatly inhibits it [39,60]. The observed variations on the catalysts' performance advocates that the basic sites required for the CO_2 activation and the RWGS also facilitates the CO adsorption and, consequently, the WGS reaction.

The incorporation of H_2O into the H_2/CO_2 feed stream resulted in drops of the CO productivity for all samples. Among them, the CO productivity of Fe-Mg/B-CDC progressively decreases as H_2O content increases being inactive with the addition of 20% of H_2O. Thus, the electron transfer cause by B atoms could provoke stronger adsorption of H^+/OH^- species limiting available active sites [39]. On the other hand, although the activities of Fe-Mg/CDC and Fe-Mg/N-CDC decrease with the addition of 3% of H_2O, the CO productivities are conserved at higher percentages of H_2O. The fact that Fe-Mg/N-CDC is more resistance against H_2O must be related with the amount of Mg present on the surface per atom of Fe (Mg/Fe) since Mg strongly adsorbs H_2O molecules in comparison with other basic promoters [61] which is beneficial for WGS reaction.

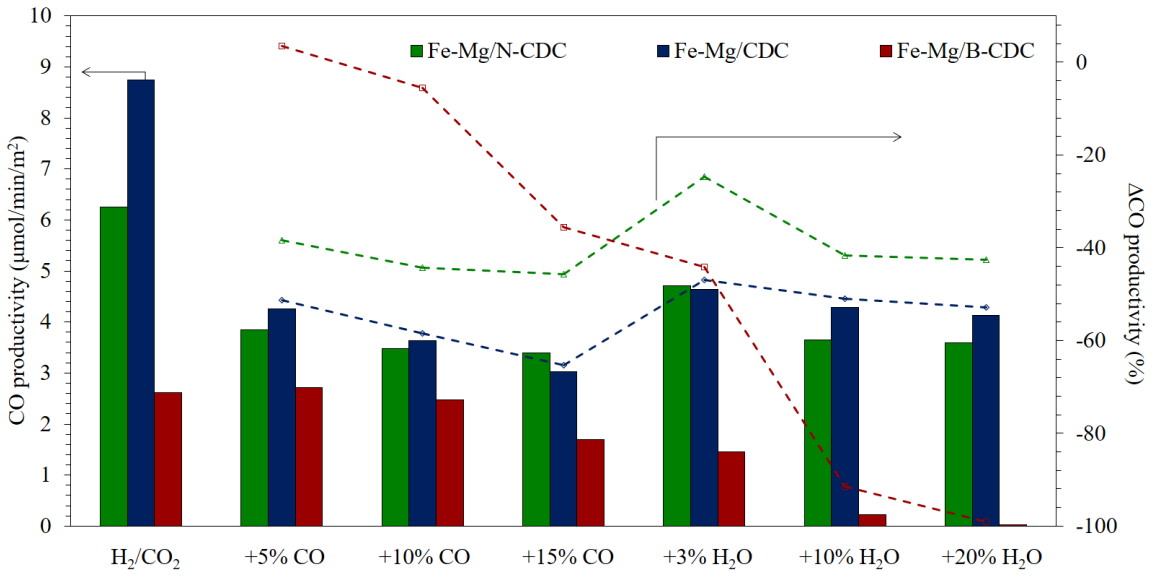

Fig. 7. Catalytic activity feeding 60%H_2 and 15%CO_2 (H_2/CO_2) in addition to CO or H_2O at 12000 h^{-1} and 500 ºC along with its variation respect to H_2/CO_2 feed.

4. Conclusions

The impact of hydrophobicity on the performance of RWGS catalysts intended at the valorization of CO_2-rich feedstock' containing CO/H_2O shares was investigated. Using Fe-Mg catalysts, three different cellulose derived carbon (CDC) supports: pristine, N-doped and B-doped CDC were employed. The characterization of the catalysts shows that metallic Fe (10 *wt*.%) and MgO (10 *wt*.%) nanoparticles are well dispersed on the carbonaceous supports. In the case of Fe-Mg/B-CDC sample, the characterization results show that B_2O_3 remains on the surface after their preparation, which are partially clogging the pores, reducing both the surface area and pore volume. CO_2-TPD results shows that Fe-Mg/CDC sample presents higher basic site density and metal content in the surface.

The activity of the catalysts was measured under RWGS conditions (500 °C, H_2/CO_2 = 4/1) and the impact of CO and H_2O species as co-reactants in the feed was evaluated. Fe-Mg/CDC reaches higher CO productivity under model conditions (CO_2/H_2) most likely due to its higher basicity. In the presence of CO, the electronic properties of the Fe-Mg/CDC catalyst seem to also promote CO adsorption thereby depleting its RWGS performance. On the contrary, CO adsorption is greatly inhibited by B_2O_3 enabling less accused drops on the CO_2 conversion

values. On the other hand, the presence of water provokes a major impact in Fe-Mg/B-CDC since electron deficiency on Fe and Mg could lead to stronger adsorption of H^+/OH^- species on the catalyst.

These results open a potential route to improve not only the RWGS reaction itself, but also the resistance of the catalysts against the presence of CO and H_2O which are common by-products, for instance, in syngas production by biomass-gasification.

CRediT authorship contribution statement

P. Tarifa: Conceptualization, Investigation, Data curation, Formal Analysis, Methodology, Writing - Original Draft, Visualization; **M. González-Castaño**: Conceptualization, Data curation, Formal Analysis, Methodology, Writing - Review & Editing, Supervision, Project administration, Funding acquisition; **F. Cazaña:** Investigation, Data curation; **A. Monzón:** Funding acquisition, Resources, Writing - Review & Editing; **H. Arellano-García:** Writing - Review & Editing, Resources, Project administration, Funding acquisition.

Declaration of Competing Interest

The authors declare no conflict of interest

Acknowledgements

This work was supported by the Spanish Ministry of Science and Innovation (MICINN, Madrid, Spain, Grant PID2020-113809RB-C31) and BTU Cottbus-Senftenberg Flagship Fellowship.

References

[1] V. Dieterich, A. Buttler, A. Hanel, H. Spliethoff, S. Fendt, Power-to-liquid via synthesis of methanol, DME or Fischer-Tropsch-fuels: a review, Energy Environ. Sci. 13 (2020) 3207. https://doi.org/10.1039/d0ee01187h.

[2] M. González-Castaño, B. Dorneanu, H. Arellano-García, The reverse water gas shift

reaction: A process systems engineering perspective, React. Chem. Eng. 6 (2021) 954–976. https://doi.org/10.1039/d0re00478b.

[3] P. Tarifa, C. Megías-Sayago, F. Cazaña, M. González-Martín, N. Latorre, E. Romeo, J.J. Delgado, A. Monzón, Highly active Ce- And Mg-promoted Ni catalysts supported on cellulose-derived carbon for low-temperature CO2 methanation, Energy and Fuels. 35 (2021) 17212–17224. https://doi.org/10.1021/acs.energyfuels.1c01682.

[4] H. Zhan, X. Shi, B. Tang, G. Wang, B. Ma, W. Liu, The performance of Cu/Zn/Zr catalysts of different Zr/(Cu+Zn) ratio for CO2 hydrogenation to methanol, Catal. Commun. 149 (2021) 106264. https://doi.org/10.1016/j.catcom.2020.106264.

[5] J. Liu, K. Li, Y. Song, C. Song, X. Guo, Selective Hydrogenation of CO2 to Hydrocarbons: Effects of Fe3O4 Particle Size on Reduction, Carburization, and Catalytic Performance, Energy and Fuels. 35 (2021) 10703–10709. https://doi.org/10.1021/acs.energyfuels.1c01265.

[6] H. Bahruji, R.D. Armstrong, J. Ruiz Esquius, W. Jones, M. Bowker, G.J. Hutchings, Hydrogenation of CO2 to Dimethyl Ether over Brønsted Acidic PdZn Catalysts, Ind. Eng. Chem. Res. 57 (2018) 6821–6829. https://doi.org/10.1021/acs.iecr.8b00230.

[7] Y.A. Daza, J.N. Kuhn, CO2 conversion by reverse water gas shift catalysis: Comparison of catalysts, mechanisms and their consequences for CO2 conversion to liquid fuels, RSC Adv. 6 (2016) 49675–49691. https://doi.org/10.1039/c6ra05414e.

[8] E. Schwab, A. Milanov, S.A. Schunk, A. Behrens, N. Schödel, Dry reforming and reverse water gas shift: Alternatives for syngas production?, Chemie-Ingenieur-Technik. 87 (2015) 347–353. https://doi.org/10.1002/cite.201400111.

[9] S.R. Foit, I.C. Vinke, L.G.J. de Haart, R.A. Eichel, Power-to-Syngas: An Enabling Technology for the Transition of the Energy System?, Angew. Chemie - Int. Ed. 56 (2017) 5402–5411. https://doi.org/10.1002/anie.201607552.

[10] P. Tarifa, T. Ramirez Reina, M. González-Castaño, H. Arellano-García, Catalytic

Upgrading of Biomass-Gasification Mixtures Using Ni-Fe/MgAl2O4 as a Bifunctional Catalyst, Energy and Fuels. 36 (2022) 8267–8273. https://doi.org/10.1021/acs.energyfuels.2c01452.

[11] M. Marchese, G. Buffo, M. Santarelli, A. Lanzini, CO2 from direct air capture as carbon feedstock for Fischer-Tropsch chemicals and fuels: Energy and economic analysis, J. CO2 Util. 46 (2021) 101487. https://doi.org/10.1016/j.jcou.2021.101487.

[12] P.S. Sai Prasad, J.W. Bae, K.W. Jun, K.W. Lee, Fischer-Tropsch synthesis by carbon dioxide hydrogenation on Fe-based catalysts, Catal. Surv. from Asia. 12 (2008) 170–183. https://doi.org/10.1007/s10563-008-9049-1.

[13] V. Garcilaso de la Vega-González, Aprovechamiento de gas no convencional en procesos GTL, Universidad de Sevilla, 2018.

[14] L. Wang, C.L. Weller, D.D. Jones, M.A. Hanna, Contemporary issues in thermal gasification of biomass and its application to electricity and fuel production, Biomass and Bioenergy. 32 (2008) 573–581. https://doi.org/10.1016/J.BIOMBIOE.2007.12.007.

[15] M. Lapuerta, J.J. Hernández, A. Pazo, J. López, Gasification and co-gasification of biomass wastes: Effect of the biomass origin and the gasifier operating conditions, Fuel Process. Technol. 89 (2008) 828–837. https://doi.org/10.1016/J.FUPROC.2008.02.001.

[16] Y. Zhao, S. Sun, H. Zhou, R. Sun, H. Tian, J. Luan, J. Qian, Experimental study on sawdust air gasification in an entrained-flow reactor, Fuel Process. Technol. 91 (2010) 910–914. https://doi.org/10.1016/J.FUPROC.2010.01.012.

[17] R. Rauch, J. Hrbek, H. Hofbauer, Biomass gasification for synthesis gas production and applications of the syngas, Wiley Interdiscip. Rev. Energy Environ. 3 (2014) 343–362. https://doi.org/10.1002/wene.97.

[18] L. Cao, I.K.M. Yu, X. Xiong, D.C.W. Tsang, S. Zhang, J.H. Clark, C. Hu, Y.H. Ng, J. Shang, Y.S. Ok, Biorenewable hydrogen production through biomass gasification: A review and future prospects, Environ. Res. 186 (2020) 109547.

https://doi.org/10.1016/j.envres.2020.109547.

[19] Y. Shen, X. Li, Z. Yao, X. Cui, C.H. Wang, CO2 gasification of woody biomass: Experimental study from a lab-scale reactor to a small-scale autothermal gasifier, Energy. 170 (2019) 497–506. https://doi.org/10.1016/j.energy.2018.12.176.

[20] J. Li, K.G. Burra, Z. Wang, X. Liu, A.K. Gupta, Syngas evolution and energy efficiency in CO2 assisted gasification of ion-exchanged pine wood, Fuel. 317 (2022) 123549. https://doi.org/10.1016/j.fuel.2022.123549.

[21] E. Shayan, V. Zare, I. Mirzaee, Hydrogen production from biomass gasification; a theoretical comparison of using different gasification agents, Energy Convers. Manag. 159 (2018) 30–41. https://doi.org/10.1016/J.ENCONMAN.2017.12.096.

[22] H. Song, G. Yang, P. Xue, Y. Li, J. Zou, S. Wang, H. Yang, H. Chen, Recent development of biomass gasification for H2 rich gas production, Appl. Energy Combust. Sci. 10 (2022) 100059. https://doi.org/10.1016/J.JAECS.2022.100059.

[23] A. Devi, A. Singh, S. Bajar, D. Pant, Z.U. Din, Ethanol from lignocellulosic biomass: An in-depth analysis of pre-treatment methods, fermentation approaches and detoxification processes, J. Environ. Chem. Eng. 9 (2021) 105798. https://doi.org/10.1016/J.JECE.2021.105798.

[24] J. Kainthola, A.S. Kalamdhad, V. V. Goud, A review on enhanced biogas production from anaerobic digestion of lignocellulosic biomass by different enhancement techniques, Process Biochem. 84 (2019) 81–90. https://doi.org/10.1016/J.PROCBIO.2019.05.023.

[25] T. Kan, V. Strezov, T.J. Evans, Lignocellulosic biomass pyrolysis: A review of product properties and effects of pyrolysis parameters, Renew. Sustain. Energy Rev. 57 (2016) 1126–1140. https://doi.org/10.1016/J.RSER.2015.12.185.

[26] Ö. Tezer, N. Karabağ, A. Öngen, C.Ö. Çolpan, A. Ayol, Biomass gasification for sustainable energy production: A review, Int. J. Hydrogen Energy. 47 (2022) 15419–

15433. https://doi.org/10.1016/J.IJHYDENE.2022.02.158.

[27] V. Kirubakaran, V. Sivaramakrishnan, R. Nalini, T. Sekar, M. Premalatha, P. Subramanian, A review on gasification of biomass, Renew. Sustain. Energy Rev. 13 (2009) 179–186. https://doi.org/10.1016/j.rser.2007.07.001.

[28] J. González-Arias, M. González-Castaño, M.E. Sánchez, J. Cara-Jiménez, H. Arellano-García, Valorization of biomass-derived CO2 residues with Cu-MnOx catalysts for RWGS reaction, Renew. Energy. 182 (2022) 443–451. https://doi.org/10.1016/j.renene.2021.10.029.

[29] M. González-Castaño, J. González-Arias, M.E. Sánchez, J. Cara-Jiménez, H. Arellano-García, Syngas production using CO2-rich residues: From ideal to real operating conditions, J. CO2 Util. 52 (2021) 101661. https://doi.org/10.1016/j.jcou.2021.101661.

[30] M. Gonzalez Castaño, T.R. Reina, S. Ivanova, M.A. Centeno, J.A. Odriozola, Pt vs. Au in water–gas shift reaction, J. Catal. 314 (2014) 1–9. https://doi.org/10.1016/J.JCAT.2014.03.014.

[31] T.R. Reina, M. Gonzalez-Castañ, ∇ Victor Lopez-Flores, L. Marcela Martínez, A. Zitolo, S. Ivanova, W. Xu, M.A. Centeno, J.A. Rodriguez, J.A. Odriozola, Au and Pt Remain Unoxidized on a CeO 2-Based Catalyst during the Water−Gas Shift Reaction, J. Am. Chem. Soc. 144 (2022) 31. https://doi.org/10.1021/jacs.1c10481.

[32] M.D.J. and D.M. David L. Williamson, Carmelo Herdes, Laura Torrente-Murciano, N‑ Doped Fe@CNT for Combined RWGS/FT CO2Hydrogenation, ACS Sustain. Chem. Eng. 7 (2019) 7395–7402. https://doi.org/https://doi.org/10.1021/acssuschemeng.9b00672.

[33] P. Tarifa, M. González-Castaño, F. Cazaña, A. Monzón, H. Arellano-García, Development of one-pot Cu/cellulose derived carbon catalysts for RWGS reaction, Fuel. 319 (2022) 123707. https://doi.org/10.1016/J.FUEL.2022.123707.

[34] D. Mattia, M.D. Jones, J.P. O'Byrne, O.G. Griffiths, R.E. Owen, E. Sackville, M.

McManus, P. Plucinski, Towards Carbon-Neutral CO2 Conversion to Hydrocarbons, ChemSusChem. 8 (2015) 4064–4072. https://doi.org/10.1002/cssc.201500739.

[35] B. Sun, K. Xu, L. Nguyen, M. Qiao, F.F. Tao, Preparation and Catalysis of Carbon-Supported Iron Catalysts for Fischer-Tropsch Synthesis, ChemCatChem. 4 (2012) 1498–1511. https://doi.org/10.1002/cctc.201200241.

[36] S. Sankaranarayanan, D.S. Lakshmi, S. Vivekanandhan, C. Ngamcharussrivichai, Biocarbons as emerging and sustainable hydrophobic/oleophilic sorbent materials for oil/water separation, Sustain. Mater. Technol. 28 (2021) e00268. https://doi.org/10.1016/j.susmat.2021.e00268.

[37] M. González-Castaño, J.C. Navarro de Miguel, J.H. Boelte, M.A. Centeno, O. Klepel, H. Arellano-García, Assessing the impact of textural properties in Ni–Fe catalysts for CO2 methanation performance, Microporous Mesoporous Mater. 327 (2021) 111405. https://doi.org/10.1016/j.micromeso.2021.111405.

[38] S. De, A.M. Balu, J.C. Van Der Waal, R. Luque, Biomass-derived porous carbon materials: Synthesis and catalytic applications, ChemCatChem. 7 (2015) 1608–1629. https://doi.org/10.1002/cctc.201500081.

[39] H. Wan, M. Qing, H. Wang, S. Liu, X.W. Liu, Y. Zhang, H. Gong, L. Li, W. Zhang, C. Song, X.D. Wen, Y. Yang, Y.W. Li, Promotive effect of boron oxide on the iron-based catalysts for Fischer-Tropsch synthesis, Fuel. 281 (2020) 118714. https://doi.org/10.1016/J.FUEL.2020.118714.

[40] M. González-Castaño, C. Morales, J.C. Navarro de Miguel, J.H. Boelte, O. Klepel, J.I. Flege, H. Arellano-García, Are Ni/ and Ni5Fe1/biochar catalysts suitable for synthetic natural gas production? A comparison with γ-Al2O3 supported catalysts, Green Energy Environ. (2021). https://doi.org/10.1016/j.gee.2021.05.007.

[41] L. Liu, S. (Johnathan) Tan, T. Horikawa, D.D. Do, D. Nicholson, J. Liu, Water adsorption on carbon - A review, Adv. Colloid Interface Sci. 250 (2017) 64–78.

https://doi.org/10.1016/J.CIS.2017.10.002.

[42] R. Mutschler, E. Moioli, W. Luo, N. Gallandat, A. Züttel, CO2 hydrogenation reaction over pristine Fe, Co, Ni, Cu and Al2O3 supported Ru: Comparison and determination of the activation energies, J. Catal. 366 (2018) 139–149. https://doi.org/10.1016/J.JCAT.2018.08.002.

[43] L. Pastor-Pérez, M. Shah, E. Le Saché, T.R. Reina, Improving Fe/Al2 O3 catalysts for the reverse water-gas shift reaction: On the effect of Cs as activity/selectivity promoter, Catalysts. 8 (2018) 608. https://doi.org/10.3390/catal8120608.

[44] S. Sengupta, A. Jha, P. Shende, R. Maskara, A.K. Das, Catalytic performance of Co and Ni doped Fe-based catalysts for the hydrogenation of CO2 to CO via reverse water-gas shift reaction, J. Environ. Chem. Eng. 7 (2019) 102911. https://doi.org/10.1016/J.JECE.2019.102911.

[45] Q. Zhang, L. Pastor-Pérez, Q. Wang, T. Ramirez Reina, Conversion of CO2 to added value products via rWGS using Fe-promoted catalysts: Carbide, metallic Fe or a mixture?, J. Energy Chem. 66 (2022) 635–646. https://doi.org/10.1016/j.jechem.2021.09.015.

[46] L. Yang, L. Pastor-Pérez, J.J. Villora-Pico, S. Gu, A. Sepúlveda-Escribano, T.R. Reina, CO2 valorisation via reverse water-gas shift reaction using promoted Fe/CeO2-Al2O3 catalysts: Showcasing the potential of advanced catalysts to explore new processes design, Appl. Catal. A Gen. 593 (2020) 117442. https://doi.org/10.1016/J.APCATA.2020.117442.

[47] C. Mebrahtu, F. Krebs, S. Perathoner, S. Abate, G. Centi, R. Palkovits, Hydrotalcite based Ni-Fe/(Mg, Al)O:X catalysts for CO2 methanation-tailoring Fe content for improved CO dissociation, basicity, and particle size, Catal. Sci. Technol. 8 (2018) 1016–1027. https://doi.org/10.1039/c7cy02099f.

[48] Z. Alipour, M. Rezaei, F. Meshkani, Effect of alkaline earth promoters (MgO, CaO,

and BaO) on the activity and coke formation of Ni catalysts supported on nanocrystalline Al2O3 in dry reforming of methane, J. Ind. Eng. Chem. 20 (2014) 2858–2863. https://doi.org/10.1016/j.jiec.2013.11.018.

[49] J. Zhu, A. Holmen, D. Chen, Carbon Nanomaterials in Catalysis: Proton Affinity, Chemical and Electronic Properties, and their Catalytic Consequences, ChemCatChem. 5 (2013) 378. https://doi.org/10.1002/cctc.201200471.

[50] T. Zhou, H. Wang, J. Key, S. Ji, V. Linkov, R. Wang, Highly dispersed ultrafine Pt nanoparticles on hydrophilic N-doped carbon tubes for improved methanol oxidation, RSC Adv. 3 (2013) 16949–16953. https://doi.org/10.1039/c3ra43047b.

[51] T.T. Pham, T.N. Pham, V. Chihaia, Q.A. Vu, T.T. Trinh, T.T. Pham, L. Van Thang, D.N. Son, How do the doping concentrations of N and B in graphene modify the water adsorption?, RSC Adv. 11 (2021) 19560–19568. https://doi.org/10.1039/d1ra01506k.

[52] J. Biscoe, B.E. Warren, An x-ray study of carbon black, J. Appl. Phys. 13 (1942) 364–371. https://doi.org/10.1063/1.1714879.

[53] M.A. Fraga, E. Jordão, M.J. Mendes, M.M.A. Freitas, J.L. Faria, J.L. Figueiredo, Properties of carbon-supported platinum catalysts: Role of carbon surface sites, J. Catal. 209 (2002) 355–364. https://doi.org/10.1006/jcat.2002.3637.

[54] H.F. Gorgulho, J.P. Mesquita, F. Gonçalves, M.F.R. Pereira, J.L. Figueiredo, Characterization of the surface chemistry of carbon materials by potentiometric titrations and temperature-programmed desorption, Carbon N. Y. 46 (2008) 1544–1555. https://doi.org/10.1016/j.carbon.2008.06.045.

[55] P. Kaspar, D. Sobola, R. Dallaev, S. Ramazanov, A. Nebojsa, S. Rezaee, L. Grmela, Characterization of Fe2O3 thin film on highly oriented pyrolytic graphite by AFM, Ellipsometry and XPS, Appl. Surf. Sci. 493 (2019) 673–678. https://doi.org/10.1016/J.APSUSC.2019.07.058.

[56] V.K. Mittal, S. Bera, R. Nithya, M.P. Srinivasan, S. Velmurugan, S. V. Narasimhan,

Solid state synthesis of Mg–Ni ferrite and characterization by XRD and XPS, J. Nucl. Mater. 335 (2004) 302–310. https://doi.org/10.1016/J.JNUCMAT.2004.05.010.

[57] M. Qing, Y. Yang, B. Wu, J. Xu, C. Zhang, P. Gao, Y. Li, Modification of Fe–SiO2 interaction with zirconia for iron-based Fischer–Tropsch catalysts, J. Catal. 279 (2011) 111–122. https://doi.org/10.1016/J.JCAT.2011.01.005.

[58] Y.C.G. Kwan, G.M. Ng, C.H.A. Huan, Identification of functional groups and determination of carboxyl formation temperature in graphene oxide using the XPS O 1s spectrum, Thin Solid Films. 590 (2015) 40–48. https://doi.org/10.1016/J.TSF.2015.07.051.

[59] J. Lu, L. Yang, B. Xu, Q. Wu, D. Zhang, S. Yuan, Y. Zhai, X. Wang, Y. Fan, Z. Hu, Promotion effects of nitrogen doping into carbon nanotubes on supported iron fischer-tropsch catalysts for lower olefins, ACS Catal. 4 (2014) 613–621. https://doi.org/10.1021/cs400931z.

[60] S.L.A. and A.N.A. Mai-Anh Ha, Eric T. Baxter, Ashley C. Cass, Boron Switch for Selectivity of Catalytic dehydrogenation on size-selected Pt clusters on Al2O3., J. Am. Chem. Soc. 139 (2017) 11568–11575. https://doi.org/https://doi.org/10.1021/jacs.7b05894.

[61] T. Baidya, R.J. Cattolica, R. Seiser, High performance Ni-Fe-Mg catalyst for tar removal in producer gas, Appl. Catal. A Gen. 558 (2018) 131–139. https://doi.org/10.1016/j.apcata.2018.03.026.

Manuscript Click here to view linked References

Hydrophobic RWGS catalysts: valorization of CO_2-rich streams in presence of CO/H_2O

P. Tarifa[a,b], M. González-Castaño[a], F. Cazaña[b], A. Monzón[b], H. Arellano-García[a].

[a] Department of Process and Plant Technology. Brandenburg University of Technology (BTU) Cottbus-Senftenberg, Platz der Deutschen 1, 03046 Cottbus, Germany

[b] Department of Chemical and Environmental Engineering, Institute of Nanoscience and Materials of Aragón (INMA), CSIC-University of Zaragoza, E-50018 Zaragoza, Spain

corresponding author: ptarifa@unizar.es, gonzalez@b-tu.de

Keywords: Reverse Water Gas Shift, biogas, H_2O, Fe catalysts, hydrophobic, doped-carbon supports.

Abstract

Nowadays, the majority of the Reverse Water Gas Shift (RWGS) studies assume somehow *model* feedstock (diluted CO_2/H_2) for syngas production. Nonetheless, biogas streams contain certain amounts of CO/H_2O which will decrease the obtained CO_2 conversion values by promoting the forward WGS reaction. Since the rate limiting step for the WGS reaction concerns the water splitting, this work proposes the use of hydrophobic RWGS catalysts as an effective strategy for the valorization of CO_2-rich feedstock in presence of H_2O and CO. Over Fe-Mg catalysts, the different hydrophilicities attained over pristine, N- and B-doped carbonaceous supports accounted for the impact on the activity of the catalyst in presence of CO/H_2O. Overall, the higher CO productivity (4.12 μmol/(min·m^2)) attained by Fe-Mg/CDC in presence of 20% of H_2O relates to hindered water adsorption and unveil the use of hydrophobic surfaces as a suitable approach for avoiding costly pre-conditioning units for the valorization of CO_2-rich streams based on RWGS processes in presence of CO/H_2O.

1. Introduction

Syngas is a key compound for the industrial production of multiple chemicals such as ammonia, alcohol, ethanol, acetic acid, or formaldehyde in addition to synthetic fuel [1–7]. The depletion of conventional sources such as natural gas, liquid hydrocarbons, fossil oil or coal [2,8,9] along with the associated carbon footprint characteristics of the traditional production routes motivate the need for the development of alternative and more sustainable sources of syngas. Biogas constitutes one such an unconventional and renewable source that has the potential to enable a delocalized conversion of CO_2-rich residues into syngas mixtures. Coupling thermocatalytic CO_2 valorization units to biogas streams derived from biomass treatment plants represents one of the central strategies projected towards the implementation of more sustainable energy systems [2–6]. In this frame, the combination of Reverse Water Gas Shift (RWGS) with Fischer-Tropsch reaction units has been proposed the most economically feasible process towards the generation of syngas [10–12].

RWGS is an endothermic equilibrium reaction in which CO_2 and H_2 are converted into CO along with H_2O molecules ($CO_2+H_2=CO+H_2O$) at temperatures higher than 700 ºC. Currently, the vast majority of RWGS studies devoted to the development of long-life efficient catalysts considers *model* feedstock composed by diluted CO_2/H_2 [13,14]. Nevertheless, although only in lower concentrations, biogas streams contain several side components like CH_4, CO, and H_2O in concentrations depending on the biomass source as well as the treatment [15–22]. For instance, disregarding Sulphur compounds and particulate matter, the average biogas composition derived from gasification units (recognized as the most easily scalable technology for biomass treatment) might be envisaged in a range of 8-57%CO_2, 5-40%CO, 3-50%H_2, 0-20%CH_4, 7-17%H_2O and N_2 [10,23–27]. Thus, insights into the influence of minor compounds commonly present in biogas should enable the design of catalytic systems capable of operating under more realistic feedstock and reducing the number of pre-conditioning units required for the biogas valorization. Recently, González-Arias [28] evaluated the performance of Cu-MnO_x

based catalysts under *model* and simulated biomass-derived streams (22% CO_2,66% H_2, 1% CO, 1% CH_4 and N_2 balanced). Different optimal MnO_x contents were found depending on the reaction atmosphere. Thus, compared to *model* feedstock (22% CO_2, 66% H_2), higher amounts of MnO_x maintained higher conversion values in presence of CH_4/CO fractions most likely due to improved resistances against coking phenomena.

Therefore, the incorporation of adequate amounts of redox promoters enhanced the performance of the RWGS catalysts under simulated biomass-derived feedstocks [28,29]. However, the CO_2 conversion drops observed in presence of CO were also associated to favored forward WGS reaction, in concordance to Le Chatelier principle. A potential strategy for constricting the negative impact that CO and H_2O induces over the CO_2 conversion values might rely on inhibiting the adsorption of the reactants on the catalyst surface and, in consequence, the forward WGS reaction. Given that the rate limiting step of the WGS reaction involves the water dissociation step, the use of a hydrophobic system should inhibit the extent at which the WGS reaction occurs, permitting higher CO_2 conversion rates [30,31].

In this sense, the use of carbonaceous supports like CNT, activated carbon, carbon spheres or Cellulose Derived Carbon (CDC) arises as an appealing approach. Being widely proposed as catalytic supports [3,32–35], carbon materials remain cost-effective and can be easily prepared from biomass conferring a renewable character [36]. Remarkably, the easily tunable textural properties [37] and functionalities of CDC supports provide tools for specific design of the catalyst depending on the final application [38]. Thus, the incorporation of heteroatoms combined to adequate surface treatments tailor the type and concentration of functional oxygenated groups affecting the acid-base or hydrophobic character thereby governing the overall catalyst behavior [32,39–41].

This study investigates the use of hydrophobic RWGS supported catalysts as an approach for the valorization of biogas streams containing H_2O and CO as undesired constituents. Among the different metals usually proposed for the RWGS reaction (Cu and Fe) [42], Fe was preferred

because of its cost-effectiveness, optimal activity and selectivity and higher thermal stability. [2,43–47]. Moreover, Mg was added as electronic promoter so the CO_2 adsorption and coke resistance were indorsed [48]. The hydrophobicity of the systems was tuned by doping the CDC supports with N and B species [49–51]. Hence, (10 wt.%)Fe-(10 wt.%)Mg catalysts supported over pristine, N-doped and B-doped CDC supports were prepared and tested for the RWGS reaction in absence and presence of H_2O and CO impurities. The chosen H_2O and CO percentages were extrapolated considering biogas feedstock derived from gasification processes. The lower conversion drops exhibited by the N-doped CDC catalyst emphasize that tailoring the hydrophobic character of the catalysts constitutes an optimal strategy towards the development of RWGS catalysts with higher tolerances towards CO/H_2O fractions.

2. Experimental

2.1. Synthesis of the catalysts

The samples were prepared by wetness impregnation of cellulose (fibers cellulose from *Sigma Aldrich*) with an aqueous dissolution with $Fe(NO_3)_3 \cdot 9H_2O$ from *Sigma Aldrich* and $Mg(NO_3)_2 \cdot 6H_2O$ from *Panreac* as metal precursors. The metal loading was fixed at 3.5%wt. of Fe with respect to the dried cellulose, along with an atomic ratio of Fe:Mg=3:7. After the impregnation, the solid was placed in a horizontal furnace and dried at 100 °C for 12 h in 50 mL/min of N_2. Afterwards, thermal decomposition was carried out under reducing atmosphere (50% H_2 balanced with N_2) at 700 °C for 3 h using a heating rate of 50 °C/min. Upon cooling down, the catalyst was passivated under N_2 overnight followed by a mixture of 16% of CO_2 (balanced with N_2 with a total flow of 250 mL/min) for 1 h. This catalyst was labelled as Fe-Mg/CDC. In addition, hydrophobic and hydrophilic catalysts were prepared adding urea or boric acid to the aqueous dissolution (6 g of urea crystal from *Panreac* and 1.6g of boric acid from *STREM Chemicals*, respectively). Then, the solid was treated following the steps

previously described. In this case, the catalysts were labelled as Fe-Mg/N-CDC and Fe-Mg/B-CDC, respectively.

2.2.Characterization techniques

The metal content of the samples was measured by inductively coupled plasma mass spectrometry (ICP-MS) with Thermo Scientific equipment. The metal content was also evaluated by TGA-Air analysis. The determination of C, H and N content on the catalysts was carried out using a Leco CHN628 elemental analyzer. The thermal stability was analyzed in Air using a METTLER Toledo STA/SDTA 851e thermogravimetric instrument. The TGA-Air experiments were conducted using around 1 mg of sample placed in a 40 μL crucible. Then, the sample was heated up to 900 ºC with a heating rate of 10 ºC/min. Since carbonaceous support is burned off under oxidative atmosphere, the metallic percentage of the samples was calculated from the weight of the remaining ashes assuming elements at their higher oxidation state (Fe_2O_3, MgO and B_2O_3 in each case). Given that the nominal molar ratio of the metal precursors used during the catalyst preparation is known, the composition of the catalysts was estimated.

XRD diffractograms were obtained by a Siemens D-5000 (45 kV, 40 mA) diffractometer equipped with Cu anode (kα radiation, λ=0,1542 nm). The diffractograms were acquired in the 5º to 90º 2θ range with 0.02º counting step and a step time of 4 s. The phase composition was determined by using an ICDD database and the High Score Plus (PANalytical) software. The crystallite size (CS) of each species was calculated using the Scherrer's equation [52].

The textural properties of the samples were analyzed by N_2 adsorption-desorption isotherms carried out at 77 K using a Tristar 3000 equipment from *Micromeritics Instrument Corp*. The surface area was calculated through Brunauer−Emmett−Teller (BET) method. On the other hand, the total pore volume along with the average pore diameter were obtained by the Horváth−Kawazoe method, while the *t*-plot method was employed to determine the

microporous volume. Finally, Barrett-Joyner-Halenda (BJH) method was used to obtain the pore size distribution.

Scanning electron microscopy (SEM) micrograph images were captured in a FEI Inspect F50 microscope operating at 10 kV microscope. Moreover, transmission electron microscopy (TEM) micrograph images were acquired in a FEI Tecnai T-20 microscope operating at 200kV.

CO_2-TPD analyses (Temperature Programmed Desorption) were performed in a ChemBet PULSAR from *Quantachrome instruments*. 50 mg of sample were placed in a U-shape reactor. Over the pre-reduced samples cooled down in inert atmosphere, CO_2 was adsorbed at room temperature exposing the sample to a flow of 15% CO_2 diluted with He for 40 min. The CO_2 specie physisorbed were removed in He flow. Afterwards, CO_2-TPD was carried out heating up to 700 °C with a heating rate of 15 °C/min. The TCD as well as mass spectrometer signals with mass-to-charge ratio (m/z) of 2, 4, 15, 28 and 44 were acquired continuously.

The chemical composition of the surface was analyzed by X-ray photoelectron spectroscopy (XPS) in a Kratos Axis ULTRA spectrometer using non-monochromatic Al Kα radiation (hν = 1486.7 eV). The spectra were analyzed using CASA XPS software by applying a Shirley-type background.

The reducibility of the samples was analyzed by Temperature Programme Reduction (TPR) in a ChemBet equipment from Anton Paar. 50 mg of sample was charged in U-shape quartz reactor. The samples were heated from room temperature up to 900 ºC at 10 ºC/min using 10% of H_2 balanced with He. TCD and mass spectrometer signals with mass-to-charge ratio (m/z) of 2, 4, 15, 28 and 44 were recorded continuously.

2.3.Catalytic activity

The catalysts diluted with SiC were placed in a fixed-bed tubular reactor (8 mm of inner diameter). The amount of catalysts was calculated in order to maintain the CO_2/ Fe ratio constant (CO_2 molar flow/Fe mass was fixed to 3.02 mol $CO_2 \cdot g_{Fe}^{-1} \cdot h^{-1}$) being GHSV 12000 h^{-1} in all cases. Prior to the reaction, the catalyst was reduced at 700 °C for 1 h using 40% of

H_2 balanced with N_2 (100 mL/min of total flow). Afterwards, the reaction was carried out at 500 °C feeding 15% of CO_2 and 60% of H_2 in all cases. In addition to that, between 3-15% of CO or 5-20% of H_2O were also co-fed. The composition of the exhausted gases was analyzed by a gas chromatographer model HP 6890 equipped with a ShinCarbon ST column. The CO productivity was calculated through the Eq.1. Additionally, the impact of CO and H_2O in the activity was calculated as the variation of the productivity respect to the CO productivity obtained under H_2/CO_2 streams following the Eq.2.

$$CO\ productivity\left(\frac{\mu mol}{\min \cdot m^2}\right) = \frac{F_{CO,\text{out}}}{m_{cat} \cdot S_{BET}} \quad \text{(Eq 1)}$$

$$\Delta CO\ productivity(\%) = \frac{CO\ prod._{\text{CO/H}_2O} - CO\ prod._{H_2/CO_2}}{CO\ prod._{H_2/CO_2}} \quad \text{(Eq 2)}$$

3. Results and discussion

3.1 Chemical and structural composition of the fresh catalysts

Table 1 shows the chemical composition obtained for the samples. According to TGA, the decomposition of the impregnated cellulose results in metal percentages higher than the nominal ones (3.5%wt. Fe and 3.6%wt. Mg) resulting in ca. 10%wt. of Fe along with 10%wt. of Mg in all cases. The Fe percentage obtained by ICP results are very close to that confirming the metallic content in the final catalysts. In addition to that, in Table 1 elemental analysis results are also included. As we can see, C and H are quite similar in all samples seeing little differences. On the contrary, Fe-Mg/B-CDC contains 5.89% of B while the N content is higher in Fe-Mg/N-CDC due to the addition of these precursors in the synthesis. In comparison with bare supports, CDC is composed mainly by carbon (see Table SI.1) while N-CDC and B-CDC show higher percentage of O due to the presence of N and B species.

Table 1. Chemical composition and elemental analysis of the fresh catalysts.

Catalyst	Fe[a] (*wt*.%)	Fe[b] (*wt*.%)	Mg[a] (*wt*.%)	B[a] (*wt*.%)	C[c] (*wt*.%)	H[c] (*wt*.%)	N[c] (*wt*.%)	O[d] (*wt*.%)
Fe-Mg/N-CDC	10.4	9.2	10.5	-	53.40	1.49	2.48	21.73
Fe-Mg/CDC	13.3	12.3	13.5	-	48.27	1.39	0.55	22.99
Fe-Mg/B-CDC	9.6	7.5	9.7	5.89	54.36	1.10	0.71	18.64

[a]weight percentages obtained from TGA-Air data
[b]weight percentages obtained from ICP measurements
[c]weight percentage obtained from elemental analysis
[d] weight percentage obtained from mass balance

In addition, the structural composition was analyzed by XRD. The diffractograms displayed in Fig. 1 show common peaks located at 44.7°, 65.0° and 82.3° attributed to metallic Fe along with peaks at 36.1°, 43.0° and 62.0° which correspond to MgO. Also, a broad peak located around 26.1° corresponds to amorphous carbonaceous support, which also appears in all catalysts. Moreover, peaks located at 43.5º, 50.6º and 74.2º are shown in Fe-Mg/B-CDC diffractogram which are attributed to $Fe_{0.94}C_{0.06}$. Regarding heteroatom addition, no nitrogen species are shown in Fe-Mg/N-CDC whereas two peaks appear in the case of Fe-Mg/B-CDC. These peaks, located at 33.5° and 19.9°, correspond to B_2O_3. This fact is due to the N species which are not introduced into the carbon lattice being removed as NO_x volatile compounds. Nevertheless, in case of boric acid, the excess of B-species remains in the catalyst as B_2O_3. In Table 2, the metallic crystal sizes calculated through Scherrer's equation are presented. Thus, metallic Fe as well as MgO manifest similar average crystal size around 38 nm and 8 nm, respectively, in as-prepared catalysts. This indicates that N or B have no significant effect on the dispersion of the metallic nanoparticles.

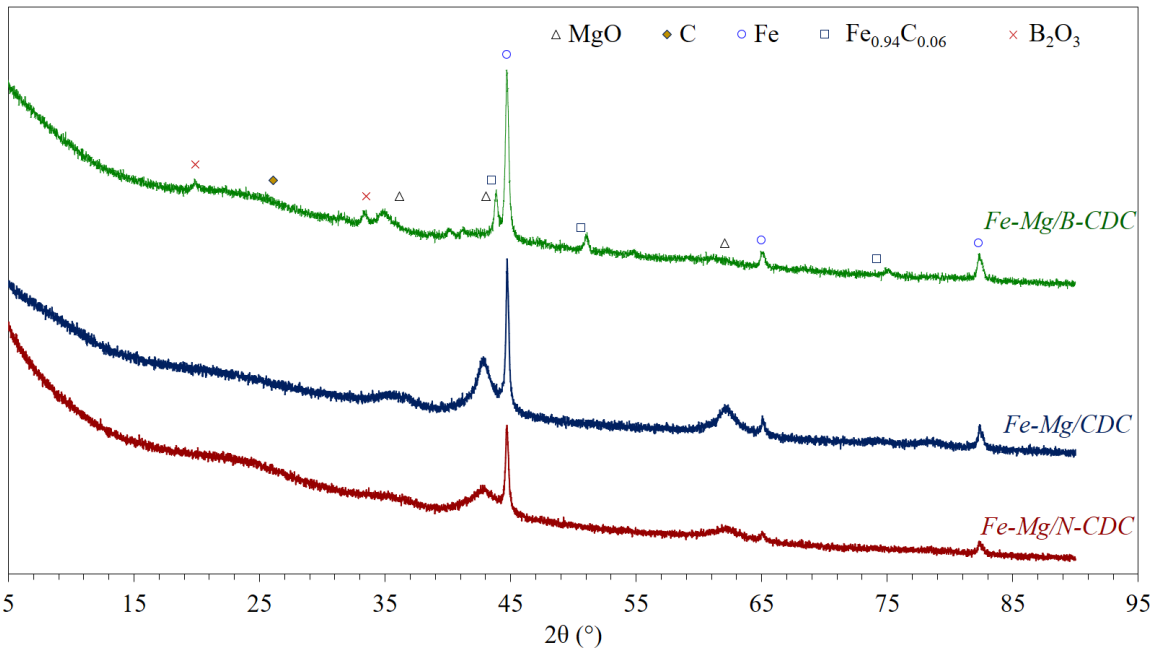

Fig. 1. XRD of the fresh catalysts.

3.2 Textural properties and micrographs of the fresh catalysts

Textural properties were analyzed by N_2 adsorption isotherms and the values obtained are presented in Table 2. Accordingly, the catalysts showed a high surface area and pore volume obtaining minimum values of 320 m^2/g and 0.291 cm^3/g, respectively, with Fe-Mg/B-CDC. In comparison with bare supports, the surface area of Fe-Mg/CDC decreases (see Table SI.1) while, in presence of N or B, surface area of the corresponding catalyst significantly increases due to metals favor the cellulose decomposition. Furthermore, the pore volume distribution displayed in Fig. 2 showed that the catalysts are mainly mesoporous materials. Thus, in comparison with Fe-Mg/CDC, Fe-Mg/N-CDC developed higher surface area as well as microporosity showing smaller average pore diameter, 1.1 nm. On the other hand, although Fe-Mg/B-CDC showed similar microporosity and average pore diameter to Fe-Mg/CDC, its surface area and pore volume decreases likely due to B-species (B_2O_3) provokes a partial block of porosity.

Table 2. Crystal size and textural properties of the fresh catalysts

	Crystal size	Textural properties

Catalyst	Fe[a] (nm)	MgO[a] (nm)	S_{BET} (m^2/g)	Pore volume (cm^3/g)	Micropore volume (%)	d_{pore} (nm)
Fe-Mg/N-CDC	38	8	436	0.330	33	1.1
Fe-Mg/CDC	41	10	388	0.374	25	2.7
Fe-Mg/B-CDC	32	7[b]	320	0.291	28	2.4

[a]calculated through Scherrer equation applied to the peak located at 44.7° for Fe and 43.0° for MgO
[b]calculated through Scherrer equation applied to the peak located at 36.1°

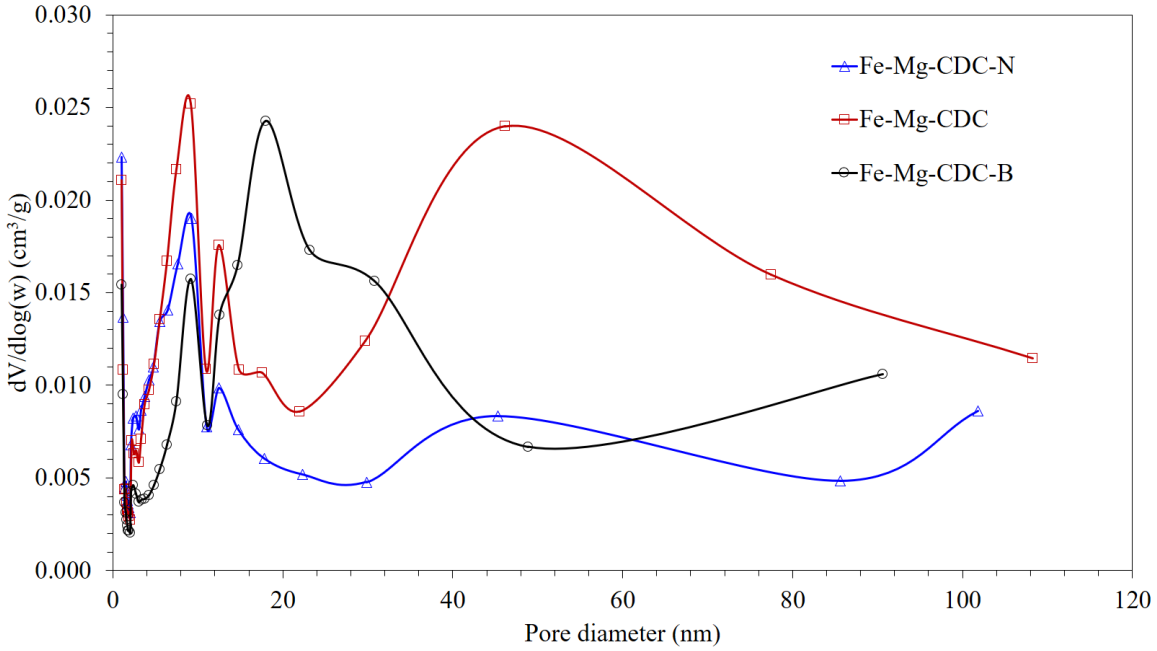

Fig. 2. Pore volume distribution of the fresh catalysts.

SEM images of the fresh catalysts are presented on the left side of Fig.3. There, Fe-Mg/N-CDC (Fig. 3A) revealed a series of intricate cavities on its surface whereas the surfaces of Fe-Mg/CDC and Fe-Mg/B-CDC are softer. Nevertheless, a higher scale image of Fe-Mg/B-CDC (Fig. 3C inset, scale of 1µm) revealed small spheres dispersed on the surface likely corresponding to B_2O_3. On the other hand, despite the differences in the macrostructure, TEM images (shown on the right side of Fig.3) and EDS-STEM results (shown in Fig. SI.1) show that the metallic nanoparticles are well dispersed on the carbonaceous support in all cases. These results are in concordance with the N_2 adsorption results as well as XRD diffractograms discussed previously.

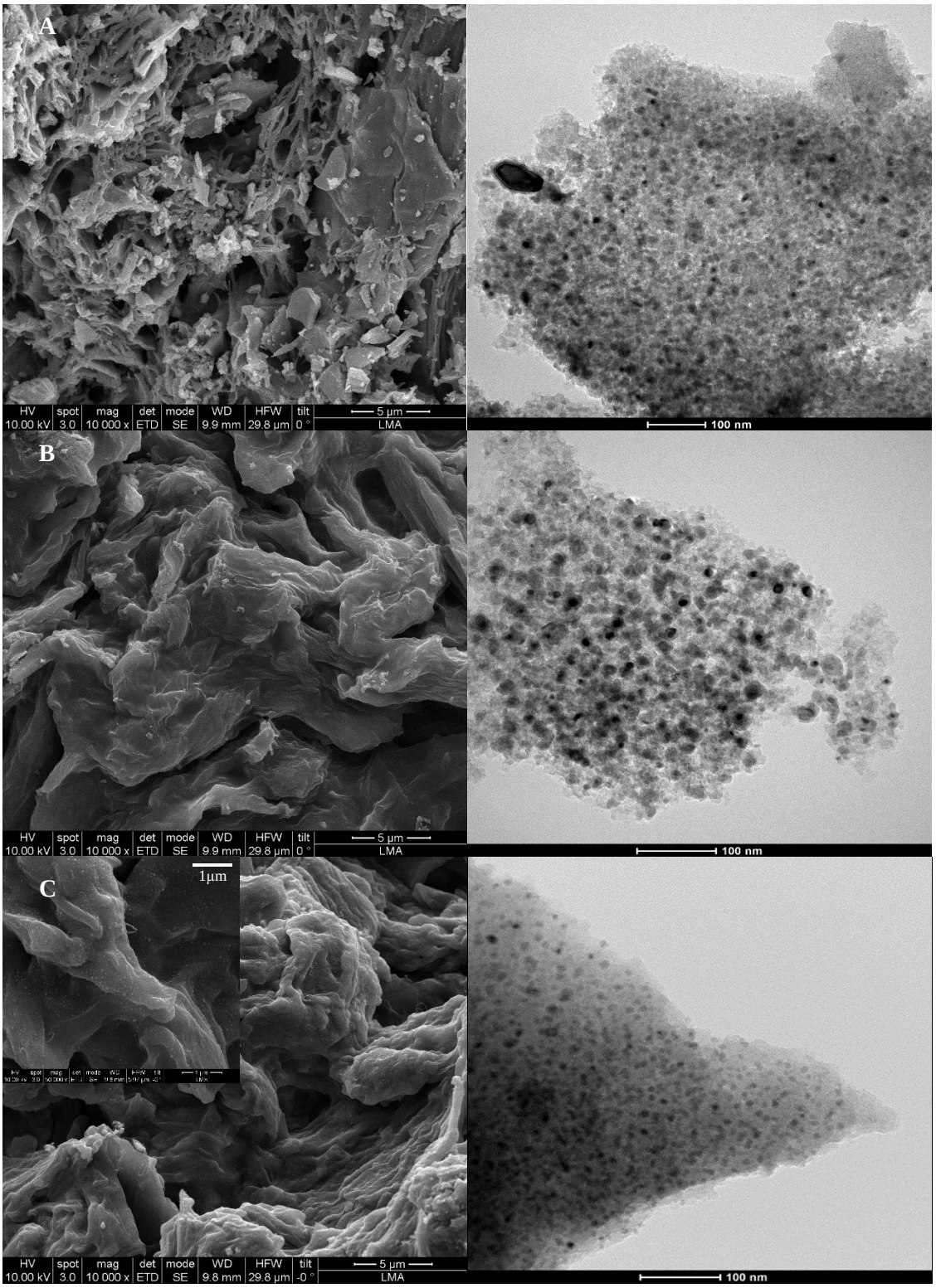

Fig. 3. SEM (left) and TEM (right) images of fresh catalysts: (A) Fe-Mg/N-CDC, (B) Fe-Mg/CDC and (C) Fe-Mg/B-CDC.

3.3 Chemical and redox properties

The CO_2-TPD were used to measure the basicity of the pre-reduced catalysts. In carbon materials, CO_2 and CO are released from the decomposition of the surface oxygen functional groups (OFGs). CO_2 is released at lower temperatures and it is related with acid sites while CO is atributted to basic sites and it appears at higher temperatures [40,53]. Specifically, CO_2 results from carboxylic acids, carboxylic anhydrides and lactones being lactone group more thermally stable. Likewise, CO results from carboxylic anhydrides, phenols, carbonyls and quinone groups [54]. In this work, carboxylic anhydrides were discarded due to CO_2 and CO signals are not overlapped. For Fe-Mg/CDC and Fe-Mg/N-CDC, the observed CO_2 desorption profiles (zoomed in Fig. 4 inset) exhibited a single broad peak located at *ca.* 300 °C which can be ascribed to carboxylic groups and underline the presence of relatively weak adsorption sites. However, the main CO_2 desorption peak observed for the Fe-Mg/B-CDC sample points to moderate-strenght sites and could be associated to the decomposition of lactone species. On the other hand, all samples exhibited a CO broad peak (no shown in supports, Fig.SI.2) from 600ºC composed by two contributions attributed to phenol and carbonyl groups. In case of Fe-Mg/B-CDC, a broader CO peak indicates the presence of stronger sites. Table 3 summarizes the quantification of the CO_2 and CO released along with the basic site density of each catalyst calculated from the CO evolved. Fe-Mg/CDC presents higher basic site density than Fe-Mg/N-CDC likely due to a low content of N remained in the carbon lattice as a result of the high temperature used in the synthesis as is corroborated by XPS results, Fig. 5.

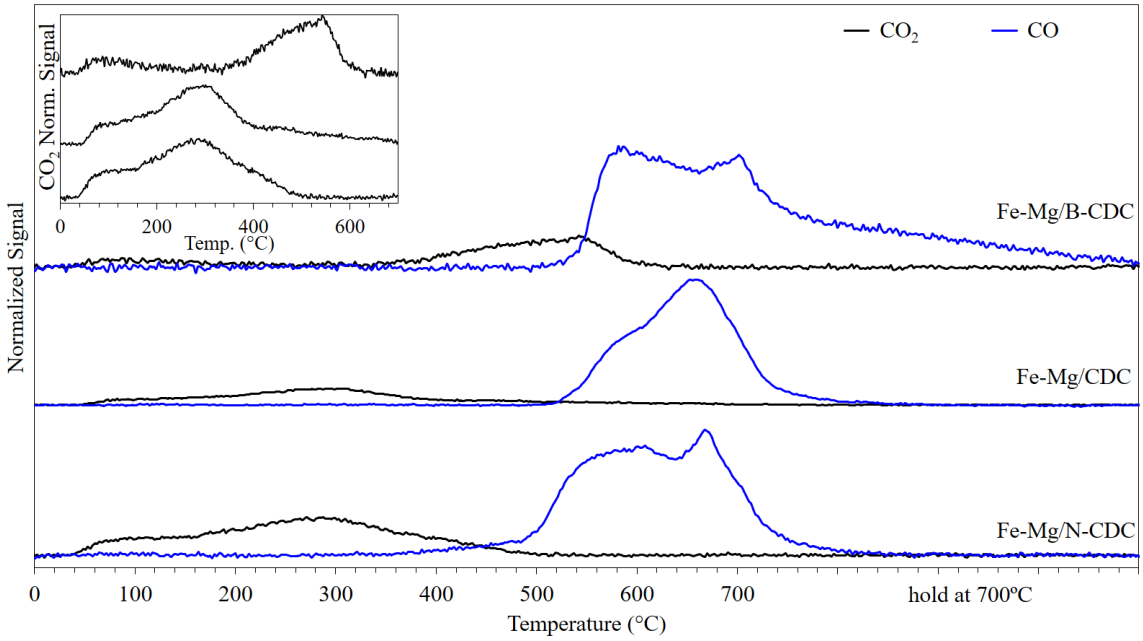

Fig. 4. Normalized CO_2 and CO evolution resulted from CO_2-TPD analysis of the reduced catalysts.

Table 3. Quantification of CO_2-TPD carried out over the pre-reduced catalysts.

Catalyst	Total CO_2 (µmol/g)	Total CO (µmol/g)	Basic site density (µmol/m^2)
Fe-Mg/N-CDC	98	284	0.651
Fe-Mg/CDC	101	556	1.433
Fe-Mg/B-CDC	30	155	0.484

The surface chemical state of the catalysts was identified by XPS analysis. Fig.5 shows XPS spectra of the different atoms involved in each catalyst. In addition, Table 4 shows the atomic percentage obtained from XPS spectra (*i.e.* surface percentages) and TGA-Air test (approximately *at%* bulk). As we can see in Fig. 5, the spectra of Fe 2p exhibits a pair of peaks located around 710.9 eV (Fe 2p3/2) and 724.5 eV (Fe 2p1/2) attributed to Fe^{3+} in Fe_2O_3 [55]. Likewise, the peak located around 1304.0 eV of Mg 1s spectra corresponds to Mg^{2+} [56] as well as the peak located around 193.8 eV of B 1s is attributed to B_2O_3 [39]. This is corroborated by O 1s spectra where the peaks located at 531.9 and 530.3 eV can be identified as O^{2-} from metal oxides and adsorbed O-H [57,58]. Thus, those spectra indicate that Fe, Mg as well as B are

presented as metal oxides while different C-N configurations were found. While the addition of N has low impact on Fe and Mg binding energies, B leads to a shift to higher binding energies in comparison with Fe-Mg/CDC indicating stronger interaction between those atoms. Indeed, given the higher electronegativity of boron with respect to Fe and Mg, it is produced an electron transfer from Fe and Mg to B leading to an electron deficiency in central atoms [39] which hinders CO_2 adsorption. The latter is in accordance with signals of Mg 2s and Mg KLL shown in supplementary information (Fig. SI.3). The atomic percentages, shown in Table 4, indicates that the concentration of Fe is quite low taking into account the atomic percentage in the bulk. Nevertheless, Fe content is higher in Fe-Mg/CDC catalyst. On the other hand, Mg atomic percentages are higher than Fe in all cases being higher also in Fe-Mg/CDC. These results are in concordance with CS found by XRD where Mg is much smaller than Fe and, therefore, more dispersed. Regarding the heteroatoms, only a minor part of N remains into the carbon lattice while B_2O_3 content represents 5.32% of the surface in case of Fe-Mg/B-CDC. This value is rather similar to B content in the bulk (5 %at.) indicating that B is mainly on the surface.

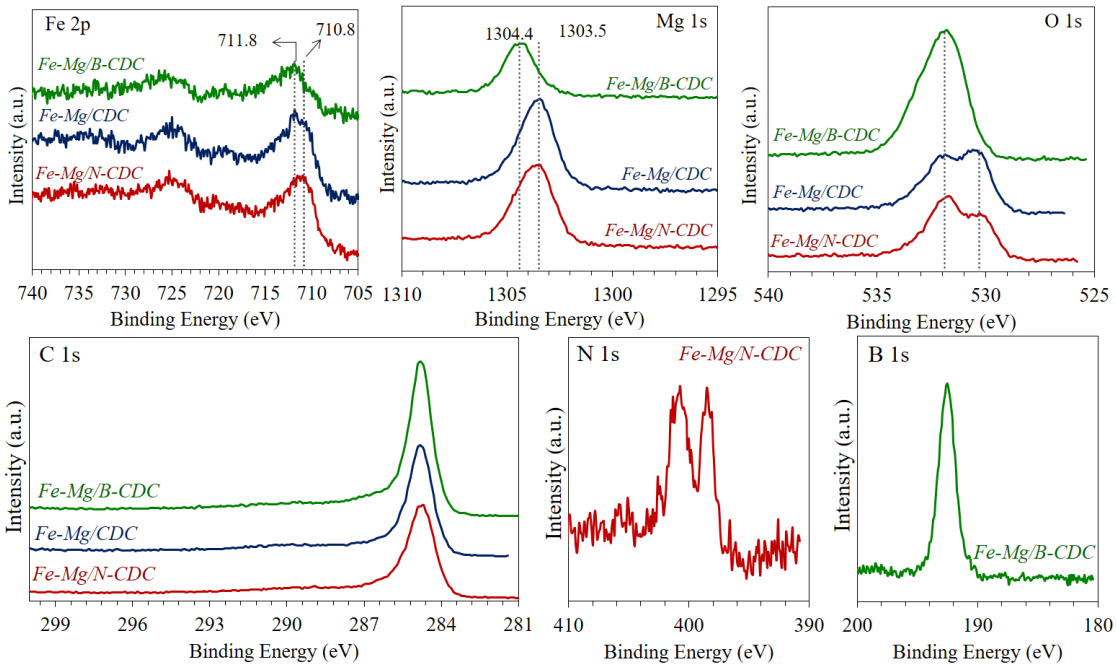

Fig. 5. XPS spectra of as-prepared catalyst.

Table 4. Surface atomic percentages of as-prepared catalyst.

Catalysts	Fe 2p (*at.%*)	Fe_{bulk} (*at.%*)	Mg 2s (*at.%*)	Mg_{bulk} (*at.%*)	C 1s (*at.%*)	O1s (*at.%*)	N or B (*at.%*)	Mg/ Fe	Fe/C ($\cdot 10^3$)
Fe-Mg/N-CDC	0.38	2.57	5.92	6.06	78.8	14.9	1.07	15.6	4.8
Fe-Mg/CDC	0.55	3.44	6.34	8.15	77.51	15.60	-	11.5	7.1
Fe-Mg/B-CDC	0.34	2.35	3.45	5.54	72.06	18.83	5.32	10	4.7

The TPR profiles of the samples are shown in Fig. 6. It is shown two peaks at around 400 and 700 ºC. According to XRD results, the peak located at 400 ºC is attributed to the reduction of Fe oxidized during the passivation since the major part of Fe remains reduced after the synthesis. Thus, the H_2 consumed in this part corresponds to less than 0.4 µmol reinforcing the latter. In addition, due to the catalysts are prepared at 700 ºC, a greater peak shown at higher temperatures is attributed to the further decomposition of the catalysts.

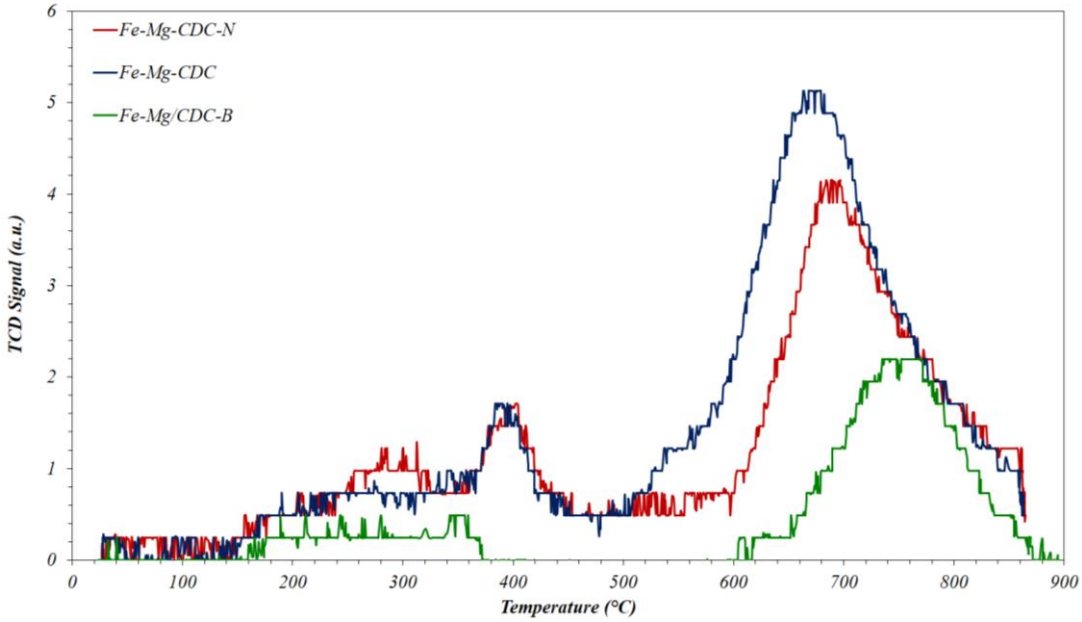

Fig. 6. TPR profiles of as-prepared catalysts.

3.4 Catalytic activity

The productivity to CO per unit of surface exhibited by the catalysts' series at 500 °C under different RWGS reaction atmospheres is shown in Fig. 7 represented by bars. In addition to that, the impact of CO/H_2O on the productivity was calculated as the variation of the

productivity respect to H_2/CO_2 feed stream productivity (dash lines). Under H_2/CO_2 feed streams, Fe-Mg/CDC exhibited higher CO productivity being these *ca*. three times higher the values reached by the Fe-Mg/B-CDC catalyst. For the RWGS reaction, the adsorption and activation of CO_2 constitutes a limiting step [2] which is indorse by basicity of the catalysts. Analogously, the poorer RWGS performance might be related to minor CO_2 adsorption cause by, on the one hand, a partial block of the basic active sites by surface B_2O_3 domains and, on the other hand, the higher binding energies showed by Fe and Mg (Fig.5). Moreover, as it was expected, the addition of CO or H_2O resulted in a drop in the CO yield since the RWGS is an equilibrium reaction and the incorporation of reaction products shift the equilibrium towards the reactants. The incorporation of CO affected in a significant manner the systems with higher RWGS activity suggesting that Fe-Mg/CDC and Fe-Mg/N-CDC samples adsorb efficiently both CO and CO_2 species. Indeed, it is well known that N-containing groups enhance the adsorption of the CO [32,59] whilst B-species greatly inhibits it [39,60]. The observed variations on the catalysts' performance advocates that the basic sites required for the CO_2 activation and the RWGS also facilitates the CO adsorption and, consequently, the WGS reaction.

The incorporation of H_2O into the H_2/CO_2 feed stream resulted in drops of the CO productivity for all samples. Among them, the CO productivity of Fe-Mg/B-CDC progressively decreases as H_2O content increases being inactive with the addition of 20% of H_2O. Thus, the electron transfer cause by B atoms could provoke stronger adsorption of H^+/OH^- species limiting available active sites [39]. On the other hand, although the activities of Fe-Mg/CDC and Fe-Mg/N-CDC decrease with the addition of 3% of H_2O, the CO productivities are conserved at higher percentages of H_2O. The fact that Fe-Mg/N-CDC is more resistance against H_2O must be related with the amount of Mg present on the surface per atom of Fe (Mg/Fe) since Mg strongly adsorbs H_2O molecules in comparison with other basic promoters [61] which is beneficial for WGS reaction.

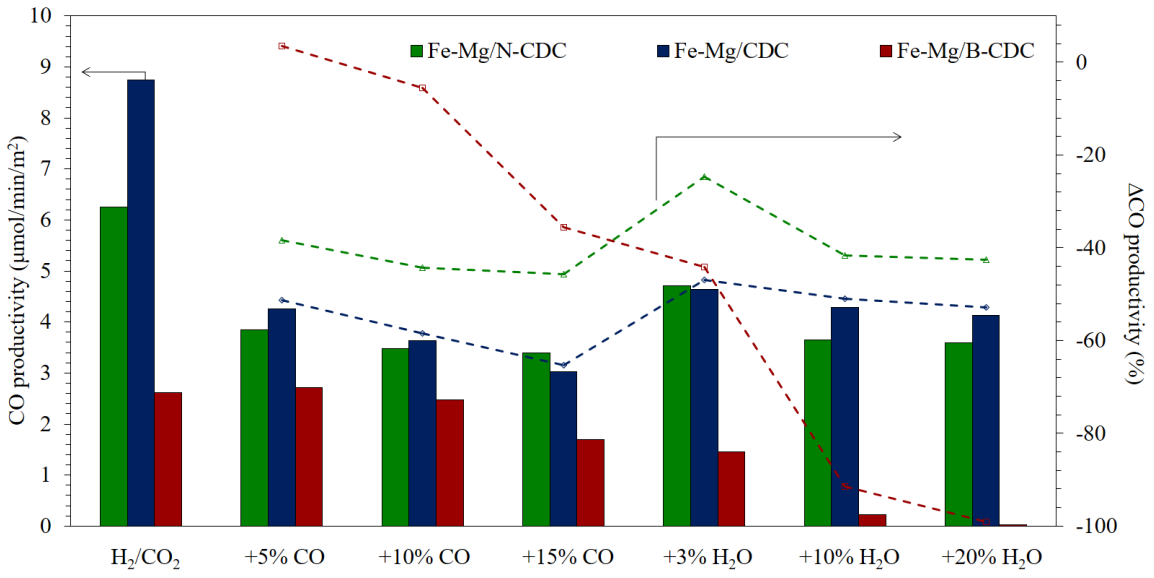

Fig. 7. Catalytic activity feeding 60%H_2 and 15%CO_2 (H_2/CO_2) in addition to CO or H_2O at 12000 h^{-1} and 500 ºC along with its variation respect to H_2/CO_2 feed.

4. Conclusions

The impact of hydrophobicity on the performance of RWGS catalysts intended at the valorization of CO_2-rich feedstock' containing CO/H_2O shares was investigated. Using Fe-Mg catalysts, three different cellulose derived carbon (CDC) supports: pristine, N-doped and B-doped CDC were employed. The characterization of the catalysts shows that metallic Fe (10 *wt*.%) and MgO (10 *wt*.%) nanoparticles are well dispersed on the carbonaceous supports. In the case of Fe-Mg/B-CDC sample, the characterization results show that B_2O_3 remains on the surface after their preparation, which are partially clogging the pores, reducing both the surface area and pore volume. CO_2-TPD results shows that Fe-Mg/CDC sample presents higher basic site density and metal content in the surface.

The activity of the catalysts was measured under RWGS conditions (500 °C, H_2/CO_2 = 4/1) and the impact of CO and H_2O species as co-reactants in the feed was evaluated. Fe-Mg/CDC reaches higher CO productivity under model conditions (CO_2/H_2) most likely due to its higher basicity. In the presence of CO, the electronic properties of the Fe-Mg/CDC catalyst seem to also promote CO adsorption thereby depleting its RWGS performance. On the contrary, CO adsorption is greatly inhibited by B_2O_3 enabling less accused drops on the CO_2 conversion

values. On the other hand, the presence of water provokes a major impact in Fe-Mg/B-CDC since electron deficiency on Fe and Mg could lead to stronger adsorption of H^+/OH^- species on the catalyst.

These results open a potential route to improve not only the RWGS reaction itself, but also the resistance of the catalysts against the presence of CO and H_2O which are common by-products, for instance, in syngas production by biomass-gasification.

CRediT authorship contribution statement

P. Tarifa: Conceptualization, Investigation, Data curation, Formal Analysis, Methodology, Writing - Original Draft, Visualization; **M. González-Castaño**: Conceptualization, Data curation, Formal Analysis, Methodology, Writing - Review & Editing, Supervision, Project administration, Funding acquisition; **F. Cazaña:** Investigation, Data curation; **A. Monzón:** Funding acquisition, Resources, Writing - Review & Editing; **H. Arellano-García:** Writing - Review & Editing, Resources, Project administration, Funding acquisition.

Declaration of Competing Interest

The authors declare no conflict of interest

Acknowledgements

This work was supported by the Spanish Ministry of Science and Innovation (MICINN, Madrid, Spain, Grant PID2020-113809RB-C31) and BTU Cottbus-Senftenberg Flagship Fellowship.

References

[1] V. Dieterich, A. Buttler, A. Hanel, H. Spliethoff, S. Fendt, Power-to-liquid via synthesis of methanol, DME or Fischer-Tropsch-fuels: a review, Energy Environ. Sci. 13 (2020) 3207. https://doi.org/10.1039/d0ee01187h.

[2] M. González-Castaño, B. Dorneanu, H. Arellano-García, The reverse water gas shift

reaction: A process systems engineering perspective, React. Chem. Eng. 6 (2021) 954–976. https://doi.org/10.1039/d0re00478b.

[3] P. Tarifa, C. Megías-Sayago, F. Cazaña, M. González-Martín, N. Latorre, E. Romeo, J.J. Delgado, A. Monzón, Highly active Ce- And Mg-promoted Ni catalysts supported on cellulose-derived carbon for low-temperature CO2 methanation, Energy and Fuels. 35 (2021) 17212–17224. https://doi.org/10.1021/acs.energyfuels.1c01682.

[4] H. Zhan, X. Shi, B. Tang, G. Wang, B. Ma, W. Liu, The performance of Cu/Zn/Zr catalysts of different Zr/(Cu+Zn) ratio for CO2 hydrogenation to methanol, Catal. Commun. 149 (2021) 106264. https://doi.org/10.1016/j.catcom.2020.106264.

[5] J. Liu, K. Li, Y. Song, C. Song, X. Guo, Selective Hydrogenation of CO2 to Hydrocarbons: Effects of Fe3O4 Particle Size on Reduction, Carburization, and Catalytic Performance, Energy and Fuels. 35 (2021) 10703–10709. https://doi.org/10.1021/acs.energyfuels.1c01265.

[6] H. Bahruji, R.D. Armstrong, J. Ruiz Esquius, W. Jones, M. Bowker, G.J. Hutchings, Hydrogenation of CO2 to Dimethyl Ether over Brønsted Acidic PdZn Catalysts, Ind. Eng. Chem. Res. 57 (2018) 6821–6829. https://doi.org/10.1021/acs.iecr.8b00230.

[7] Y.A. Daza, J.N. Kuhn, CO2 conversion by reverse water gas shift catalysis: Comparison of catalysts, mechanisms and their consequences for CO2 conversion to liquid fuels, RSC Adv. 6 (2016) 49675–49691. https://doi.org/10.1039/c6ra05414e.

[8] E. Schwab, A. Milanov, S.A. Schunk, A. Behrens, N. Schödel, Dry reforming and reverse water gas shift: Alternatives for syngas production?, Chemie-Ingenieur-Technik. 87 (2015) 347–353. https://doi.org/10.1002/cite.201400111.

[9] S.R. Foit, I.C. Vinke, L.G.J. de Haart, R.A. Eichel, Power-to-Syngas: An Enabling Technology for the Transition of the Energy System?, Angew. Chemie - Int. Ed. 56 (2017) 5402–5411. https://doi.org/10.1002/anie.201607552.

[10] P. Tarifa, T. Ramirez Reina, M. González-Castaño, H. Arellano-García, Catalytic

Upgrading of Biomass-Gasification Mixtures Using Ni-Fe/MgAl2O4 as a Bifunctional Catalyst, Energy and Fuels. 36 (2022) 8267–8273. https://doi.org/10.1021/acs.energyfuels.2c01452.

[11] M. Marchese, G. Buffo, M. Santarelli, A. Lanzini, CO2 from direct air capture as carbon feedstock for Fischer-Tropsch chemicals and fuels: Energy and economic analysis, J. CO2 Util. 46 (2021) 101487. https://doi.org/10.1016/j.jcou.2021.101487.

[12] P.S. Sai Prasad, J.W. Bae, K.W. Jun, K.W. Lee, Fischer-Tropsch synthesis by carbon dioxide hydrogenation on Fe-based catalysts, Catal. Surv. from Asia. 12 (2008) 170–183. https://doi.org/10.1007/s10563-008-9049-1.

[13] V. Garcilaso de la Vega-González, Aprovechamiento de gas no convencional en procesos GTL, Universidad de Sevilla, 2018.

[14] L. Wang, C.L. Weller, D.D. Jones, M.A. Hanna, Contemporary issues in thermal gasification of biomass and its application to electricity and fuel production, Biomass and Bioenergy. 32 (2008) 573–581. https://doi.org/10.1016/J.BIOMBIOE.2007.12.007.

[15] M. Lapuerta, J.J. Hernández, A. Pazo, J. López, Gasification and co-gasification of biomass wastes: Effect of the biomass origin and the gasifier operating conditions, Fuel Process. Technol. 89 (2008) 828–837. https://doi.org/10.1016/J.FUPROC.2008.02.001.

[16] Y. Zhao, S. Sun, H. Zhou, R. Sun, H. Tian, J. Luan, J. Qian, Experimental study on sawdust air gasification in an entrained-flow reactor, Fuel Process. Technol. 91 (2010) 910–914. https://doi.org/10.1016/J.FUPROC.2010.01.012.

[17] R. Rauch, J. Hrbek, H. Hofbauer, Biomass gasification for synthesis gas production and applications of the syngas, Wiley Interdiscip. Rev. Energy Environ. 3 (2014) 343–362. https://doi.org/10.1002/wene.97.

[18] L. Cao, I.K.M. Yu, X. Xiong, D.C.W. Tsang, S. Zhang, J.H. Clark, C. Hu, Y.H. Ng, J. Shang, Y.S. Ok, Biorenewable hydrogen production through biomass gasification: A review and future prospects, Environ. Res. 186 (2020) 109547.

https://doi.org/10.1016/j.envres.2020.109547.

[19] Y. Shen, X. Li, Z. Yao, X. Cui, C.H. Wang, CO2 gasification of woody biomass: Experimental study from a lab-scale reactor to a small-scale autothermal gasifier, Energy. 170 (2019) 497–506. https://doi.org/10.1016/j.energy.2018.12.176.

[20] J. Li, K.G. Burra, Z. Wang, X. Liu, A.K. Gupta, Syngas evolution and energy efficiency in CO2 assisted gasification of ion-exchanged pine wood, Fuel. 317 (2022) 123549. https://doi.org/10.1016/j.fuel.2022.123549.

[21] E. Shayan, V. Zare, I. Mirzaee, Hydrogen production from biomass gasification; a theoretical comparison of using different gasification agents, Energy Convers. Manag. 159 (2018) 30–41. https://doi.org/10.1016/J.ENCONMAN.2017.12.096.

[22] H. Song, G. Yang, P. Xue, Y. Li, J. Zou, S. Wang, H. Yang, H. Chen, Recent development of biomass gasification for H2 rich gas production, Appl. Energy Combust. Sci. 10 (2022) 100059. https://doi.org/10.1016/J.JAECS.2022.100059.

[23] A. Devi, A. Singh, S. Bajar, D. Pant, Z.U. Din, Ethanol from lignocellulosic biomass: An in-depth analysis of pre-treatment methods, fermentation approaches and detoxification processes, J. Environ. Chem. Eng. 9 (2021) 105798. https://doi.org/10.1016/J.JECE.2021.105798.

[24] J. Kainthola, A.S. Kalamdhad, V. V. Goud, A review on enhanced biogas production from anaerobic digestion of lignocellulosic biomass by different enhancement techniques, Process Biochem. 84 (2019) 81–90. https://doi.org/10.1016/J.PROCBIO.2019.05.023.

[25] T. Kan, V. Strezov, T.J. Evans, Lignocellulosic biomass pyrolysis: A review of product properties and effects of pyrolysis parameters, Renew. Sustain. Energy Rev. 57 (2016) 1126–1140. https://doi.org/10.1016/J.RSER.2015.12.185.

[26] Ö. Tezer, N. Karabağ, A. Öngen, C.Ö. Çolpan, A. Ayol, Biomass gasification for sustainable energy production: A review, Int. J. Hydrogen Energy. 47 (2022) 15419–

15433. https://doi.org/10.1016/J.IJHYDENE.2022.02.158.

[27] V. Kirubakaran, V. Sivaramakrishnan, R. Nalini, T. Sekar, M. Premalatha, P. Subramanian, A review on gasification of biomass, Renew. Sustain. Energy Rev. 13 (2009) 179–186. https://doi.org/10.1016/j.rser.2007.07.001.

[28] J. González-Arias, M. González-Castaño, M.E. Sánchez, J. Cara-Jiménez, H. Arellano-García, Valorization of biomass-derived CO2 residues with Cu-MnOx catalysts for RWGS reaction, Renew. Energy. 182 (2022) 443–451. https://doi.org/10.1016/j.renene.2021.10.029.

[29] M. González-Castaño, J. González-Arias, M.E. Sánchez, J. Cara-Jiménez, H. Arellano-García, Syngas production using CO2-rich residues: From ideal to real operating conditions, J. CO2 Util. 52 (2021) 101661. https://doi.org/10.1016/j.jcou.2021.101661.

[30] M. Gonzalez Castaño, T.R. Reina, S. Ivanova, M.A. Centeno, J.A. Odriozola, Pt vs. Au in water–gas shift reaction, J. Catal. 314 (2014) 1–9. https://doi.org/10.1016/J.JCAT.2014.03.014.

[31] T.R. Reina, M. Gonzalez-Castañ, ∇ Victor Lopez-Flores, L. Marcela Martínez, A. Zitolo, S. Ivanova, W. Xu, M.A. Centeno, J.A. Rodriguez, J.A. Odriozola, Au and Pt Remain Unoxidized on a CeO 2-Based Catalyst during the Water−Gas Shift Reaction, J. Am. Chem. Soc. 144 (2022) 31. https://doi.org/10.1021/jacs.1c10481.

[32] M.D.J. and D.M. David L. Williamson, Carmelo Herdes, Laura Torrente-Murciano, N‑ Doped Fe@CNT for Combined RWGS/FT CO2Hydrogenation, ACS Sustain. Chem. Eng. 7 (2019) 7395–7402. https://doi.org/https://doi.org/10.1021/acssuschemeng.9b00672.

[33] P. Tarifa, M. González-Castaño, F. Cazaña, A. Monzón, H. Arellano-García, Development of one-pot Cu/cellulose derived carbon catalysts for RWGS reaction, Fuel. 319 (2022) 123707. https://doi.org/10.1016/J.FUEL.2022.123707.

[34] D. Mattia, M.D. Jones, J.P. O'Byrne, O.G. Griffiths, R.E. Owen, E. Sackville, M.

McManus, P. Plucinski, Towards Carbon-Neutral CO2 Conversion to Hydrocarbons, ChemSusChem. 8 (2015) 4064–4072. https://doi.org/10.1002/cssc.201500739.

[35] B. Sun, K. Xu, L. Nguyen, M. Qiao, F.F. Tao, Preparation and Catalysis of Carbon-Supported Iron Catalysts for Fischer-Tropsch Synthesis, ChemCatChem. 4 (2012) 1498–1511. https://doi.org/10.1002/cctc.201200241.

[36] S. Sankaranarayanan, D.S. Lakshmi, S. Vivekanandhan, C. Ngamcharussrivichai, Biocarbons as emerging and sustainable hydrophobic/oleophilic sorbent materials for oil/water separation, Sustain. Mater. Technol. 28 (2021) e00268. https://doi.org/10.1016/j.susmat.2021.e00268.

[37] M. González-Castaño, J.C. Navarro de Miguel, J.H. Boelte, M.A. Centeno, O. Klepel, H. Arellano-García, Assessing the impact of textural properties in Ni–Fe catalysts for CO2 methanation performance, Microporous Mesoporous Mater. 327 (2021) 111405. https://doi.org/10.1016/j.micromeso.2021.111405.

[38] S. De, A.M. Balu, J.C. Van Der Waal, R. Luque, Biomass-derived porous carbon materials: Synthesis and catalytic applications, ChemCatChem. 7 (2015) 1608–1629. https://doi.org/10.1002/cctc.201500081.

[39] H. Wan, M. Qing, H. Wang, S. Liu, X.W. Liu, Y. Zhang, H. Gong, L. Li, W. Zhang, C. Song, X.D. Wen, Y. Yang, Y.W. Li, Promotive effect of boron oxide on the iron-based catalysts for Fischer-Tropsch synthesis, Fuel. 281 (2020) 118714. https://doi.org/10.1016/J.FUEL.2020.118714.

[40] M. González-Castaño, C. Morales, J.C. Navarro de Miguel, J.H. Boelte, O. Klepel, J.I. Flege, H. Arellano-García, Are Ni/ and Ni5Fe1/biochar catalysts suitable for synthetic natural gas production? A comparison with γ-Al2O3 supported catalysts, Green Energy Environ. (2021). https://doi.org/10.1016/j.gee.2021.05.007.

[41] L. Liu, S. (Johnathan) Tan, T. Horikawa, D.D. Do, D. Nicholson, J. Liu, Water adsorption on carbon - A review, Adv. Colloid Interface Sci. 250 (2017) 64–78.

https://doi.org/10.1016/J.CIS.2017.10.002.

[42] R. Mutschler, E. Moioli, W. Luo, N. Gallandat, A. Züttel, CO2 hydrogenation reaction over pristine Fe, Co, Ni, Cu and Al2O3 supported Ru: Comparison and determination of the activation energies, J. Catal. 366 (2018) 139–149. https://doi.org/10.1016/J.JCAT.2018.08.002.

[43] L. Pastor-Pérez, M. Shah, E. Le Saché, T.R. Reina, Improving Fe/Al2 O3 catalysts for the reverse water-gas shift reaction: On the effect of Cs as activity/selectivity promoter, Catalysts. 8 (2018) 608. https://doi.org/10.3390/catal8120608.

[44] S. Sengupta, A. Jha, P. Shende, R. Maskara, A.K. Das, Catalytic performance of Co and Ni doped Fe-based catalysts for the hydrogenation of CO2 to CO via reverse water-gas shift reaction, J. Environ. Chem. Eng. 7 (2019) 102911. https://doi.org/10.1016/J.JECE.2019.102911.

[45] Q. Zhang, L. Pastor-Pérez, Q. Wang, T. Ramirez Reina, Conversion of CO2 to added value products via rWGS using Fe-promoted catalysts: Carbide, metallic Fe or a mixture?, J. Energy Chem. 66 (2022) 635–646. https://doi.org/10.1016/j.jechem.2021.09.015.

[46] L. Yang, L. Pastor-Pérez, J.J. Villora-Pico, S. Gu, A. Sepúlveda-Escribano, T.R. Reina, CO2 valorisation via reverse water-gas shift reaction using promoted Fe/CeO2-Al2O3 catalysts: Showcasing the potential of advanced catalysts to explore new processes design, Appl. Catal. A Gen. 593 (2020) 117442. https://doi.org/10.1016/J.APCATA.2020.117442.

[47] C. Mebrahtu, F. Krebs, S. Perathoner, S. Abate, G. Centi, R. Palkovits, Hydrotalcite based Ni-Fe/(Mg, Al)O:X catalysts for CO2 methanation-tailoring Fe content for improved CO dissociation, basicity, and particle size, Catal. Sci. Technol. 8 (2018) 1016–1027. https://doi.org/10.1039/c7cy02099f.

[48] Z. Alipour, M. Rezaei, F. Meshkani, Effect of alkaline earth promoters (MgO, CaO,

and BaO) on the activity and coke formation of Ni catalysts supported on nanocrystalline Al2O3 in dry reforming of methane, J. Ind. Eng. Chem. 20 (2014) 2858–2863. https://doi.org/10.1016/j.jiec.2013.11.018.

[49] J. Zhu, A. Holmen, D. Chen, Carbon Nanomaterials in Catalysis: Proton Affinity, Chemical and Electronic Properties, and their Catalytic Consequences, ChemCatChem. 5 (2013) 378. https://doi.org/10.1002/cctc.201200471.

[50] T. Zhou, H. Wang, J. Key, S. Ji, V. Linkov, R. Wang, Highly dispersed ultrafine Pt nanoparticles on hydrophilic N-doped carbon tubes for improved methanol oxidation, RSC Adv. 3 (2013) 16949–16953. https://doi.org/10.1039/c3ra43047b.

[51] T.T. Pham, T.N. Pham, V. Chihaia, Q.A. Vu, T.T. Trinh, T.T. Pham, L. Van Thang, D.N. Son, How do the doping concentrations of N and B in graphene modify the water adsorption?, RSC Adv. 11 (2021) 19560–19568. https://doi.org/10.1039/d1ra01506k.

[52] J. Biscoe, B.E. Warren, An x-ray study of carbon black, J. Appl. Phys. 13 (1942) 364–371. https://doi.org/10.1063/1.1714879.

[53] M.A. Fraga, E. Jordão, M.J. Mendes, M.M.A. Freitas, J.L. Faria, J.L. Figueiredo, Properties of carbon-supported platinum catalysts: Role of carbon surface sites, J. Catal. 209 (2002) 355–364. https://doi.org/10.1006/jcat.2002.3637.

[54] H.F. Gorgulho, J.P. Mesquita, F. Gonçalves, M.F.R. Pereira, J.L. Figueiredo, Characterization of the surface chemistry of carbon materials by potentiometric titrations and temperature-programmed desorption, Carbon N. Y. 46 (2008) 1544–1555. https://doi.org/10.1016/j.carbon.2008.06.045.

[55] P. Kaspar, D. Sobola, R. Dallaev, S. Ramazanov, A. Nebojsa, S. Rezaee, L. Grmela, Characterization of Fe2O3 thin film on highly oriented pyrolytic graphite by AFM, Ellipsometry and XPS, Appl. Surf. Sci. 493 (2019) 673–678. https://doi.org/10.1016/J.APSUSC.2019.07.058.

[56] V.K. Mittal, S. Bera, R. Nithya, M.P. Srinivasan, S. Velmurugan, S. V. Narasimhan,

Solid state synthesis of Mg–Ni ferrite and characterization by XRD and XPS, J. Nucl. Mater. 335 (2004) 302–310. https://doi.org/10.1016/J.JNUCMAT.2004.05.010.

[57] M. Qing, Y. Yang, B. Wu, J. Xu, C. Zhang, P. Gao, Y. Li, Modification of Fe–SiO2 interaction with zirconia for iron-based Fischer–Tropsch catalysts, J. Catal. 279 (2011) 111–122. https://doi.org/10.1016/J.JCAT.2011.01.005.

[58] Y.C.G. Kwan, G.M. Ng, C.H.A. Huan, Identification of functional groups and determination of carboxyl formation temperature in graphene oxide using the XPS O 1s spectrum, Thin Solid Films. 590 (2015) 40–48. https://doi.org/10.1016/J.TSF.2015.07.051.

[59] J. Lu, L. Yang, B. Xu, Q. Wu, D. Zhang, S. Yuan, Y. Zhai, X. Wang, Y. Fan, Z. Hu, Promotion effects of nitrogen doping into carbon nanotubes on supported iron fischer-tropsch catalysts for lower olefins, ACS Catal. 4 (2014) 613–621. https://doi.org/10.1021/cs400931z.

[60] S.L.A. and A.N.A. Mai-Anh Ha, Eric T. Baxter, Ashley C. Cass, Boron Switch for Selectivity of Catalytic dehydrogenation on size-selected Pt clusters on Al2O3., J. Am. Chem. Soc. 139 (2017) 11568–11575. https://doi.org/https://doi.org/10.1021/jacs.7b05894.

[61] T. Baidya, R.J. Cattolica, R. Seiser, High performance Ni-Fe-Mg catalyst for tar removal in producer gas, Appl. Catal. A Gen. 558 (2018) 131–139. https://doi.org/10.1016/j.apcata.2018.03.026.

 Click here to view linked References

Supplementary information: Hydrophobic RWGS catalysts: valorization of CO_2-rich streams in presence of CO/H_2O

P. Tarifa[a,b], M. González-Castaño[a], F. Cazaña[b], A. Monzón[b], H. Arellano-García[a].

[a] Department of Process and Plant Technology. Brandenburg University of Technology (BTU) Cottbus-Senftenberg, Platz der Deutschen 1, 03046 Cottbus, Germany

[b] Department of Chemical and Environmental Engineering, Institute of Nanoscience and Materials of Aragón (INMA), CSIC-University of Zaragoza, E-50018 Zaragoza, Spain

Table SI.1. Elemental analysis and textural properties of pristine supports.

Support	C[a] (*wt.*%)	H[a] (*wt.*%)	N[a] (*wt.*%)	B[b] (*wt.*%)	O[c] (*wt.*%)	S_{BET} (m^2/g)	Pore volume (cm^3/g)	Micropore volume (%)	d_{pore} (nm)
N-CDC	88.24	2.12	4.52	-	5.12	7	0.019	17	1.1
CDC	95.07	1.43	0.59	-	2.91	482	0.219	87	1.1
B-CDC	74.93	1.65	0.40	6.89	16.13	2	0.002	49	13.4

[a]weight percentage obtained from elemental analysis
[b]weight percentage obtained from TGA-Air data
[c] weight percentage obtained from mass balance

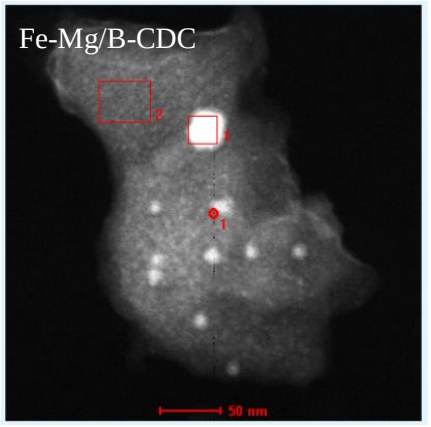

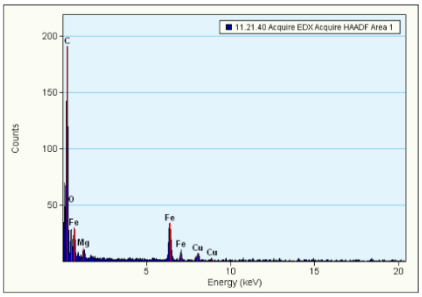

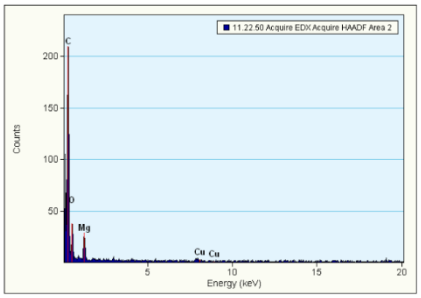

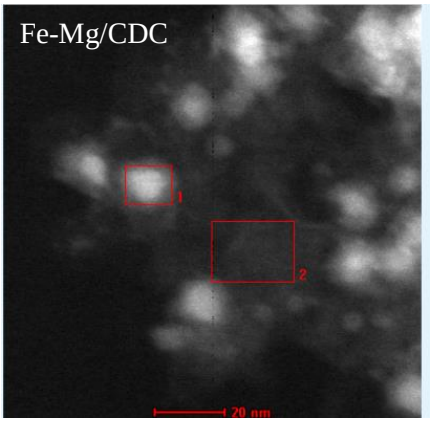

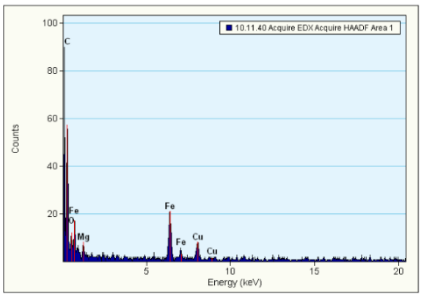

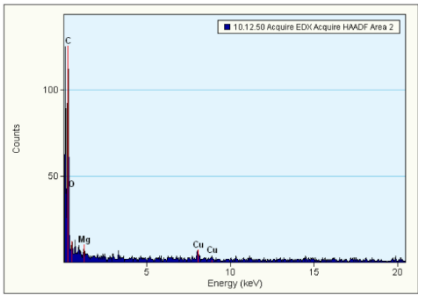

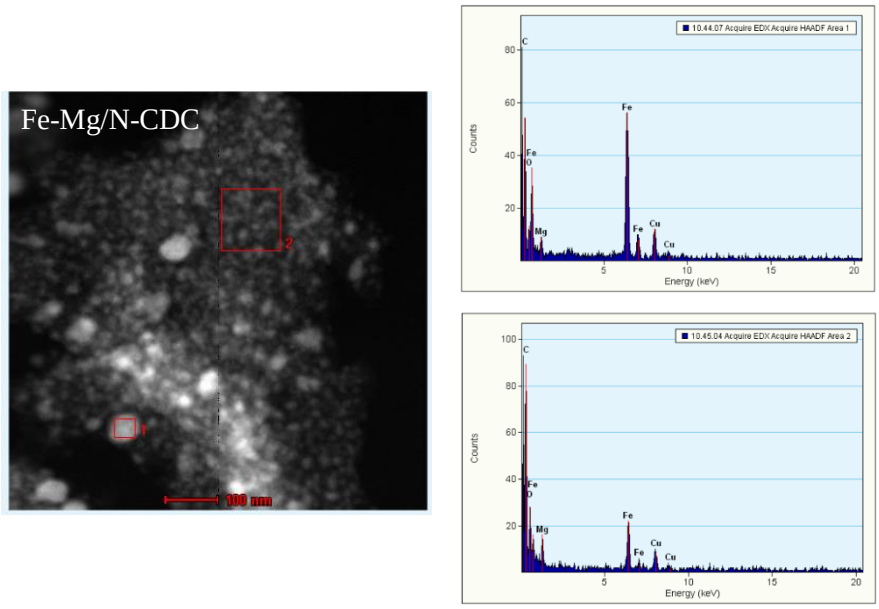

Fig SI.1. EDS-STEM analysis acquired from the designed areas of as-prepared catalysts. Bigger nanoparticles of Fe surrounded by Mg are found along with smaller nanoparticles Mg highly dispersed on the support.

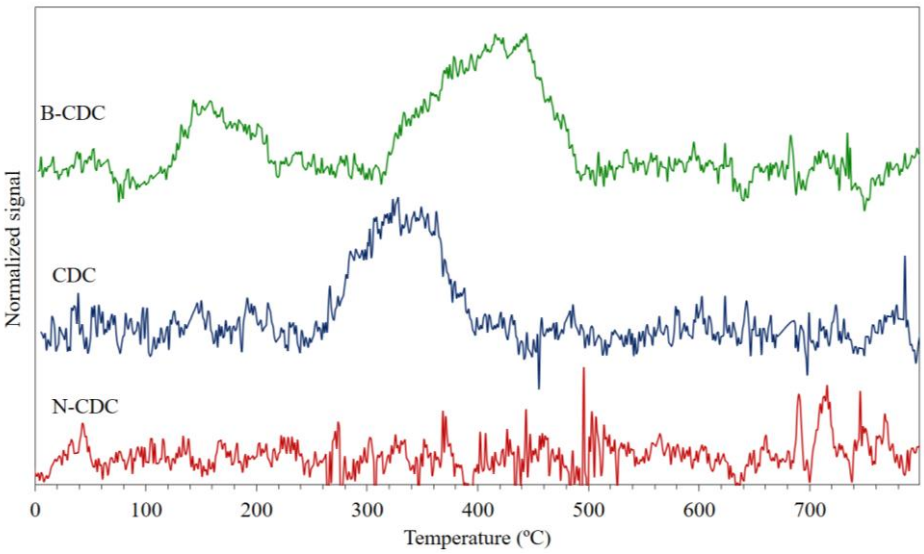

Fig SI.2. Normalized CO_2 profile resulted from CO_2-TPD analysis of the reduced supports. The amount of CO_2 desorbed was 10 µmol/g in case of B-CDC and 4 µmol/g in case of CDC.

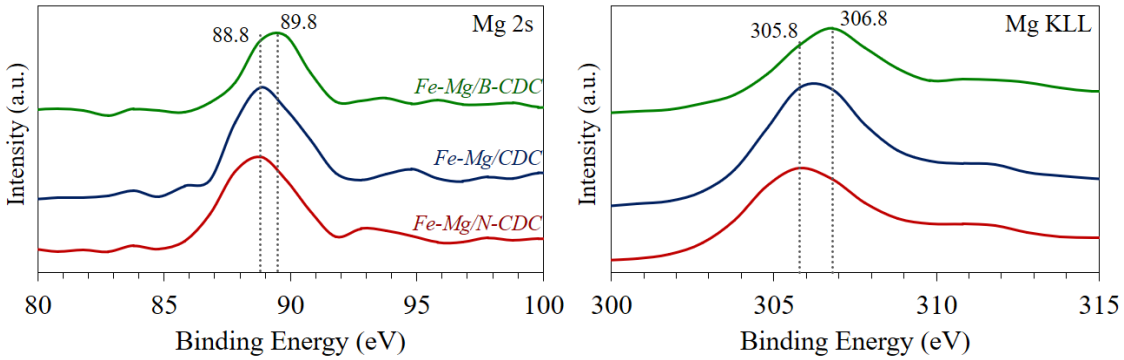

Fig SI.3. XPS spectra of Mg 2s and satellite signal of as-prepared catalyst.

CRediT authorship contribution statement

P. Tarifa: Conceptualization, Investigation, Data curation, Formal Analysis, Methodology, Writing - Original Draft, Visualization;

M. González-Castaño: Conceptualization, Data curation, Formal Analysis, Methodology, Writing - Review & Editing, Supervision, Project administration, Funding acquisition;

F. Cazaña: Investigation, Data curation;

A. Monzón: Funding acquisition, Resources, Writing - Review & Editing;

H. Arellano-García: Writing - Review & Editing, Resources, Project administration, Funding acquisition.

Declaration of interests

☒The authors declare that they have no known competing financial interests or personal relationships that could have appeared to influence the work reported in this paper.

☐The authors declare the following financial interests/personal relationships which may be considered as potential competing interests: